NASA TECHNICAL MEMORANDUM

NASA TM X-2560

NASA TM X-2560

A COMPARISON OF THEORETICAL PREDICTIONS AND HEAT-TRANSFER MEASUREMENTS FOR A FLIGHT EXPERIMENT AT MACH 20 (REENTRY F) [U]

by P. Calvin Stainback, Charles B. Johnson, Lawrence B. Boney, and Kathleen C. Wicker

Langley Research Center

Hampton, Va. 23365

NATIONAL AERONAUTICS AND SPACE ADMINISTRATION • WASHINGTON, D. C. • JULY 1972

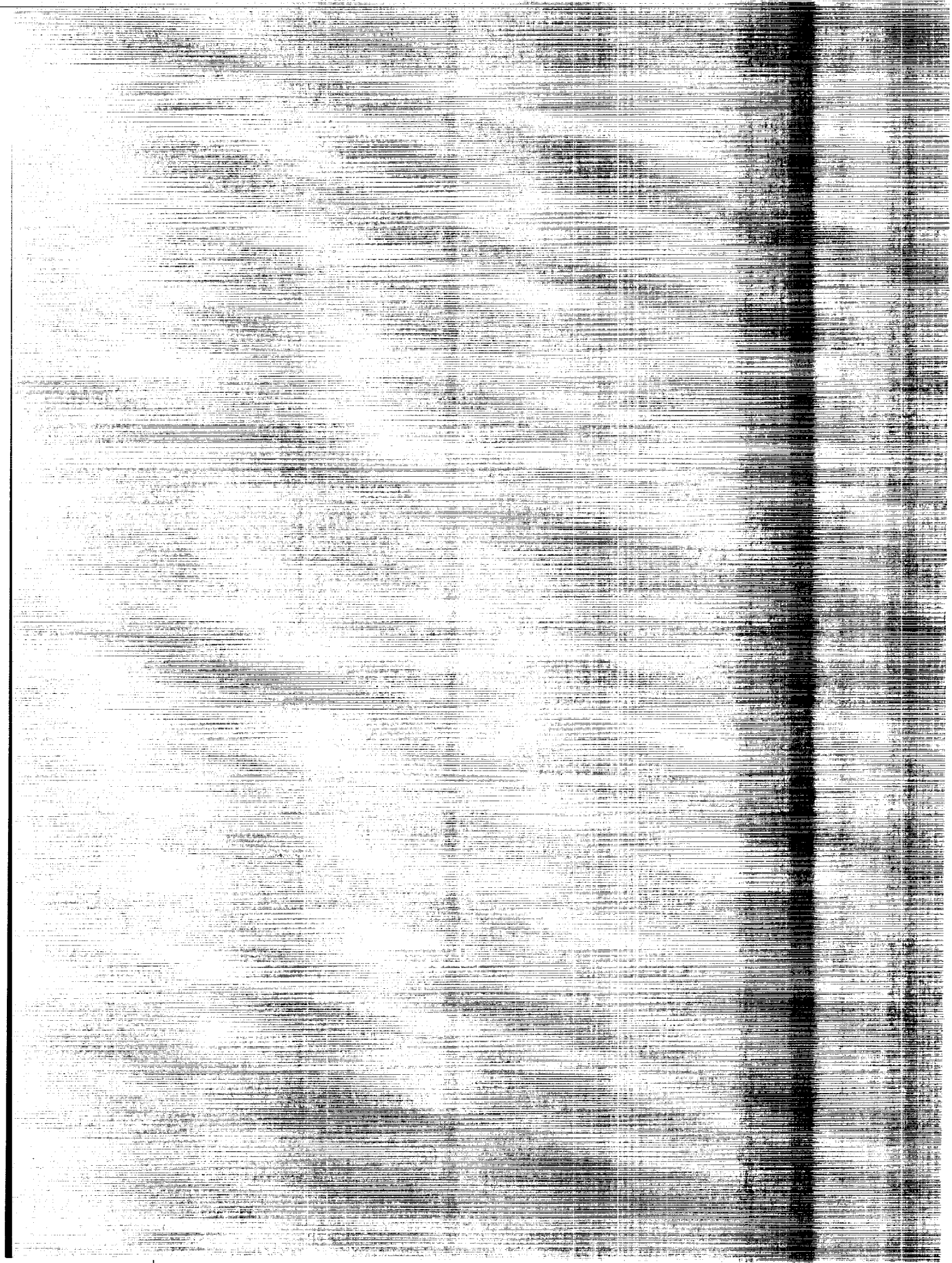

C 7 2 71972

[redacted]

1. Report No.	2. Government Accession No.	3. Recipient's Catalog No.
NASA TM X-2560		

4. Title and Subtitle	5. Report Date
A COMPARISON OF THEORETICAL PREDICTIONS AND HEAT-TRANSFER MEASUREMENTS FOR A FLIGHT EXPERIMENT AT MACH 20 (REENTRY F) (U)	July 1972
	6. Performing Organization Code
7. Author(s) P. Calvin Stainback, Charles B. Johnson, Lillian R. Boney, and Kathleen C. Wicker	8. Performing Organization Report No. L-8183
	10. Work Unit No. 136-13-04-01
9. Performing Organization Name and Address NASA Langley Research Center Hampton, Va. 23365	11. Contract or Grant No.
	13. Type of Report and Period Covered Technical Memorandum
12. Sponsoring Agency Name and Address National Aeronautics and Space Administration Washington, D.C. 20546	14. Sponsoring Agency Code

15. Supplementary Notes

16. Abstract

Predicted heating rates were compared with measured laminar, transitional, and turbulent heating rates obtained on a flight vehicle designated Reentry F. The comparisons were made over an altitude range from 36.58 to 18.29 km (120 000 to 60 000 ft) where the flight velocity was approximately 6.10 km/sec (20 000 ft/sec, Mach 20). At the higher altitudes the mean trim angle of attack was about 0.1^{o}; however, at the lowest altitude the local effective angle of attack increased to about 1.5^{o} at the most forward measuring station due to vehicle trim and thermal distortion. The measured transitional and turbulent heating rates were compared with predictions from an integral theory which used a modified tangent-cone technique. The laminar heating rates were compared with predictions from (1) linearized theory for sharp cones at angle of attack and (2) a modified tangent-cone theory.

17. Key Words (Suggested by Author(s))	18. Distribution Statement
Free flight Mach 20 Reentry F Laminar, transitional, and turbulent heating data and correlations	Confidential – Available to U.S. Government Agencies and Their Contractors Only

19. Security Classif. (of this report)	20. Security Classif. (of this page)	21. No. of Pages	22. Price
[redacted]	Unclassified	55	

[redacted]

[redacted]

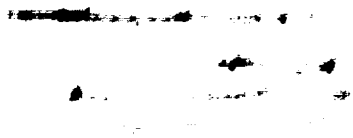

[redacted]

A COMPARISON OF THEORETICAL PREDICTIONS AND HEAT-TRANSFER MEASUREMENTS FOR A FLIGHT EXPERIMENT AT MACH 20 (REENTRY F)*

By P. Calvin Stainback, Charles B. Johnson, Lillian R. Boney, and Kathleen C. Wicker
Langley Research Center

SUMMARY

Predicted heating rates were compared with measured laminar, transitional, and turbulent heating rates obtained on a flight vehicle designated Reentry F. The comparisons were made over an altitude range from 36.58 to 18.29 km (120 000 to 60 000 ft) where the flight velocity was approximately 6.10 km/sec (20 000 ft/sec, Mach 20). At the higher altitudes the mean trim angle of attack was about 0.1°; however, at the lowest altitude the local effective angle of attack increased to about 1.5° at the most forward measuring station due to vehicle trim and thermal distortion.

The measured transitional and turbulent heating rates agreed well with the predicted rates. Laminar heating rates were in fair agreement with predictions from a linearized laminar flow theory for sharp cones at angle of attack. Predictions of laminar heating rates obtained by using a modified tangent-cone theory were poor when compared with flight and wind-tunnel data at local effective angles of attack greater than a few tenths of a degree.

INTRODUCTION

The optimum design of heat protection systems for vehicles that operate at high Mach numbers in the atmosphere requires reliable predictions of the heating rates, particularly for a transitional and turbulent boundary layer. Existing theoretical prediction methods are based on data obtained in ground facilities and limited flight experiments (refs. 1 to 3) where most of the test conditions fall significantly short of those experienced by vehicles operating at high Mach numbers.

Because of these limitations of present transitional and turbulent heat-transfer data, the Reentry F flight experiment was conducted to obtain heating-rate data at boundary-layer edge Mach numbers up to 15, total enthalpies of about 18 J/mg (8000 Btu/lb), and wall-to-total enthalpy ratios of about 0.03. These heat-transfer data can be used to eval-

*Title, Unclassified.

[redacted]

uate and to extend the range of present data correlations obtained from ground facilities and other flight experiments and also to evaluate current turbulent-boundary-layer theories (refs. 2 and 3) and guide future development of these theories.

Analyses of the heating rates measured on the Reentry F vehicles were made in references 4 and 5. The analysis presented in reference 4 was the initial evaluation of the data. A more complete analysis of the data was given in reference 5 in which the laminar and turbulent heating-rate data were compared with predictions from current correlation methods using sharp-cone conditions (also blunt-cone conditions for the laminar data) at the edge of the boundary layer. The data were also compared with preliminary results obtained by using the variable-entropy methods described in references 6, 7, and 8. The present report presents a more complete analysis of the data with these variable-entropy effects taken into account.

A limited amount of heat-transfer data obtained from wind-tunnel tests are also presented. These tests were conducted to ascertain the effects of vehicle geometry and angle of attack on heating rates and to determine whether such effects could account for the decrease of the measured Reentry F laminar heating rates with the increase in density (refs. 4 and 5). Predictions from a linearized laminar-boundary-layer theory for sharp cones at angle of attack are compared with results from the flight and wind-tunnel tests.

Several other reports have been published which describe the Reentry F vehicle and test results; some of these publications that provide basic data for the present report are references 9 to 14.

SYMBOLS

Values are given in both SI and U.S. Customary Units. The measurements and calculations were made in U.S. Customary Units.

h	altitude
M_∞	free-stream Mach number
q	heating rate
q_α	heating rate at angle of attack
$q_{\alpha=0}$	heating rate at zero angle of attack
R_S	Reynolds number based on local conditions

[redacted]

R_∞	Reynolds number based on free-stream conditions
r_n	nose radius
s	surface distance from stagnation point
$s_{t,b}$	location of the beginning of transition
$s_{t,e}$	location of the end of transition
t	wall-to-total enthalpy ratio
V_∞	free-stream velocity
x	distance from virtual origin of conical surface
α	mean trim angle of attack
α_{eff}	effective angle of attack, $\alpha + \delta$
δ	local angle of distortion
θ_c	cone angle of wind-tunnel model $(\theta_c = 5^o)$
$\theta_{c,eff}$	cone angle used to obtain surface pressures by tangent-cone theory
θ_s	cone angle for shock shape
ϕ	azimuthal angle in cylindrical coordinate system

Subscripts:

lam	laminar
turb	turbulent
w	local value at surface

[redacted]

FLIGHT VEHICLE AND TRAJECTORY

Description of Vehicle

The Reentry F flight vehicle (fig. 1), was a 5° half-angle cone 3.962 m (156 in.) long with an initial nose radius of 2.54 mm (0.100 in.). Except for the graphite nose, the vehicle was constructed from several truncated beryllium conical shells 1.542 cm (0.60 in.) thick bolted together to form the conical surface. (See ref. 10.) The nose of the vehicle, from $x = 2.44$ cm (0.96 in.) to 21.59 cm (8.5 in.), was constructed from graphite to withstand the severe heating near the apex. This nose section had an initial cone half-angle of 5.38°. This change in cone angle resulted in a 1.016-mm (0.040 in.) rearward-facing step at the graphite-beryllium junction which prevented a forward-facing step during the data acquisition period. A gap was also provided at the graphite-beryllium junction to allow for thermal expansion of the outer graphite shell of the nose. This gap tended to close during the data period. (See ref. 10 for construction details of the nose.) Dimensions of the exterior geometry of the graphite nose are shown in figure 1.

Instrumentation

The vehicle was instrumented with thermocouples at 21 stations with 12 stations located on one conical ray (fig. 1). The ray with 12 stations has been denoted the major ray. The calculations presented herein are applied mainly to this ray. A detailed description of the Reentry F instrumentation is available in reference 10.

Trajectory and Vehicle Motion

The vehicle was launched from the NASA Wallops Station on a modified Scout vehicle. The launch operation and trajectory are described in reference 10. The prime data acquisition period occurred over the altitude range from about 36.58 to 18.29 km (120 000 to 60 000 ft). However, the body motions were such that below an altitude of about 27.43 km (90 000 ft) the trim angle of attack increased, with the major thermocouple ray being continuously located on the leeward side of the body. (See ref. 11.) Consequently, the temperatures of the beryllium shell were higher along the ray opposite the major ray and, as a result, some axial distortion or bending of the vehicle occurred. The analysis of this thermal distortion is given in reference 14.

The mean trim angle of attack, as measured from the axis of symmetry of the undeformed vehicle (that is, from the axis of symmetry at the center of gravity), never exceeded 0.75° during the data acquisition period (ref. 11). However, thermal distortion increased or decreased the local inclination angle at points along the body with respect to the free-stream-velocity vector. For example, at an altitude of 18.29 km (60 000 ft) the trim angle of attack was 0.75°; however, thermal distortion increased the local angle of attack at the most forward thermocouple station ($x = 40.6$ cm or 16 in.) to 1.55°. This

angle of attack is large for a 5° cone; however, it must be noted that this angle occurred only at the most forward station for the latest time at which data have been used.

Although the main thermocouple ray was predominately leeward below an altitude of about 25.91 km (85 000 ft), it was not the most leeward ray. The mean roll angle for the main ray was about 10° for altitudes below 25.91 km (85 000 ft). (See ref. 11.) This displacement of the main ray from the most leeward position could have some slight influence on the local heating rates. The influence of angle of attack and roll on local heating is discussed in a subsequent section where ground facility test data are described.

WIND-TUNNEL INVESTIGATION

Model

In support of the Reentry F flight experiment, a wind-tunnel investigation was conducted to determine the effect of the rearward-facing step and the gap at the graphite-beryllium junction on heating and transition. The model was a 5° half-angle cone 72.4 cm (28.5 in.) long that could be tested with various nose configurations. The model was made with a longitudinal thin-skin region to measure heating in a streamwise direction. A nose having a 2.44-mm (0.096 in.) radius was used with the model to simulate the forward 72.4 cm (28.5 in.) of the Reentry F vehicle. A nose radius of 0.504 mm (0.020 in.) was used to simulate the maximum value of s/r_n for the flight vehicle.

Five nose configurations were used during the wind-tunnel tests and their pertinent data are given in the following table:

Nose configuration	r_n, mm (in.)	Surface
1	0	Smooth
2	2.54 (0.10)	Smooth
3	2.44 (0.096)	Step gap (Reentry F nose)
4	0.508 (0.020)	Step gap (Reentry F nose)
5	2.44 (0.096)	Forward-facing step (simulate failure of nose flank)

Models having smooth nose surfaces with radii of 0 and 2.54 mm (0.10 in.) were used as the reference configurations. Nose configurations having 2.44-mm (0.096 in.) and 0.508-mm (0.020 in.) radii simulated the preflight nose of the Reentry F vehicle and are the third and fourth configurations listed in the table. A fifth configuration had a forward-facing step at the graphite-beryllium station of the vehicle. This last configuration simulated a failure of the outer shell of the graphite nose that would produce a 3.56-mm (0.14 in.) forward-facing step at the graphite-beryllium junction.

[redacted]

Test Procedure and Data Reduction

The tests were conducted in the Langley Mach 8 variable-density hypersonic tunnels over a unit Reynolds number range from about 2.2×10^6 to 33×10^6 per meter (0.67×10^6 to 10.0×10^6 per foot). The tunnel operates in the blowdown mode. It has a contoured nozzle that produces a uniform Mach number of 8 in the test section at a stagnation pressure of 3.5 N/mm2 (500 psia). For lower and higher stagnation pressures, the Mach number is slightly lower and higher, respectively. For a more complete description of the tunnel, see references 15 and 16.

The model was tested over an angle-of-attack range from 0^o to 1.5^o in 0.5^o increments. For some of the tests, the thermocouples were alined on either the windward or leeward ray. Other tests were conducted with the thermocouples rolled 10^o from the most windward and leeward rays. These latter tests were made because the flight data indicated that during a significant portion of the data acquisition period the mean location of the main thermocouple ray was 10^o circumferentially from the most leeward ray.

The heating rates to the wind-tunnel model were obtained by using the calorimeter technique. The procedure was to shield the model at room temperature from the test-section flow during the time steady flow conditions were being established in the test section. After steady flow conditions were established, the model was rapidly injected into the flow. The temperature was recorded 20 times per second. The heat-transfer rates were calculated by fitting a second-degree curve to the temperature history and evaluating the change in temperature with respect to time at about 0.50 sec after model injection. Because of the early time at which data were reduced, the model was at approximately room temperature; this resulted in the data being obtained at a wall-to-total temperature ratio of about 0.40.

For further details of the testing technique and the data reduction methods, see reference 17.

RESULTS AND DISCUSSION OF FLIGHT EXPERIMENT AND COMPARISON WITH THEORY

The heat-transfer data for the flight experiment were obtained from reference 13. The theoretical method for predicting the laminar heating rates was described in reference 7. The transitional and turbulent heating method was described in reference 8. The modified tangent-cone method for including the effect of angle of attack on the laminar, transitional, and turbulent heating predictions is described in reference 6. Data and theoretical predictions are presented for the flight conditions listed in table I. These conditions represent, to good accuracy, the most probable nose radius, mean trim angle of attack, vehicle deformation, and location of the beginning and end of transition. (See refs. 4, 9, 10, 11, 12, 13, and 14.) At $h = 18.29$ km (60 000 ft) thermal distortion was

[redacted]

large near the nose of the vehicle but decreased to about 0.10° at $x = 190.5$ cm (75 in.). At this altitude, boundary-layer transition occurred near the nose and fully developed turbulent flow occurred farther rearward. Hence, two cases for different local angles of attack are presented in table I for an altitude of 18.29 km (60 000 ft). The first case listed $(\alpha_{eff} = 0.750^{\circ})$ represents the conditions assumed to be most applicable for the turbulent portion of the boundary layer. The second case $(\alpha_{eff} = 1.55^{\circ})$ represents the conditions for the station at $x = 40.6$ cm (16 in.). Since boundary-layer transition occurs near this station, it has been assumed that the second case is most applicable for the laminar boundary layer at the beginning of transition. The shock shape calculated for a 5° half-angle cone at zero angle of attack was used in all the calculations.

Laminar Tangent-Cone Theory

As shown in figure 2, the laminar-tangent-cone predictions and the flight data agreed within 25 percent at altitudes between 36.58 and 24.38 km (120 000 and 80 000 ft) where the angle of attack was always less than 0.2°. For example, at $h = 36.58$ km (120 000 ft) the data were about 15 to 25 percent greater than the theoretical values. The flight data decreased relative to the theoretical predictions as altitude decreased until at $h = 24.38$ km (80 000 ft) the flight data were about 10 percent less than the predicted values. At lower altitudes, the mean trim angle of attack increased from 0.2° to 0.75° and the flight data continued to decrease with respect to the corresponding predictions until at $h = 18.29$ km (60 000 ft) the data were only about 40 percent of the theoretical data (fig. 2(j), $s < 51$ cm (20 in.)).

The effect of thermal distortion was included in the laminar theory only at $h = 18.29$ km (60 000 ft); however, the improvement in the predictions at the other altitudes where thermal distortion should be included would be minor. Therefore, it appears that laminar boundary-layer theory based on the tangent-cone concept is inadequate to predict the laminar heating to the Reentry F vehicle when the mean trim angle of attack exceeds only a few tenths of a degree.

Linearized Laminar Theory

Because of the failure of the laminar tangent-cone theory to predict the measured heating rates, a relatively simple (but general) linearized theory for sharp cones at angles of attack (ref. 18) was used to predict the laminar flight data. The quantity $q_{\alpha}/q_{\alpha=0}$ was obtained from the theory of reference 18, and $q_{\alpha=0}$ was obtained by the method of references 6 and 7. In all the theoretical predictions, the quantity $q_{\alpha}/q_{\alpha=0}$ was calculated for the local effective angle of attack obtained from the combined mean trim angle of attack (ref. 11) and local vehicle deformation (ref. 14). The local effective angles of attack used are given in table II.

The results of these predictions are represented by dash-line curves in figure 2. For all altitudes the agreement of the data is better with the linear sharp-cone predictions than with the tangent-cone predictions. The improvement is, of course, small at high altitudes where the angle of attack is smallest. The improvement becomes significant at h = 18.29 km (60 000 ft) where the local angle of attack equals 1.55^{o} at x = 40.6 cm (16 in.). (See fig. 2(j).) At this altitude the linear theory is perhaps only 25 percent above the data, whereas the tangent-cone theory is at least 150 percent greater. The agreement between the flight data obtained from a blunt $\left(100 \leqq \frac{s}{r_n} \leqq 1000\right)$ conical vehicle and the linear theoretical predictions for a sharp cone was unexpected. The agreement may be due to the large number of nose radii downstream of the stagnation point for which the flight data were obtained and the corresponding small effect of nose bluntness for $\alpha \neq 0^{o}$. Also, variable entropy caused by the blunt nose may not have much effect on the prediction of $q_{\alpha}/q_{\alpha=0}$.

Turbulent Tangent-Cone Theory

The turbulent predictions from the integral theory used in reference 6 and described in reference 8 are from 10 to 20 percent below the data at all altitudes where fully developed turbulent flow existed on the vehicle (fig. 2). Probably the most uncertain quantity used in the turbulent flow analysis was the value of the Reynolds analogy factor. The review of Reynolds analogy factors in reference 19 illustrates the large uncertainty that exists for the variation of the Reynolds analogy factor with Mach number, wall-to-total enthalpy ratio, and other parameters. The Reynolds analogy factor used in reference 6 and discussed in reference 8 was obtained by fitting a second-degree curve to the data of reference 19. The equation was assumed to be valid over the range of wall-to-total enthalpy ratios from 0.2 to 0.65; for values below 0.2 the Reynolds analogy factor was assumed to be 1.0. The wall-to-total enthalpy ratio for the Reentry F flight was about 0.05; therefore, the Reynolds analogy factor for the present calculations shown in figure 2 was 1.0. Because of the scatter in the available Reynolds analogy factor data, it is highly probable that the value of 1.0 is low. If the Reynolds analogy factor is increased by 10 percent to a value of 1.1, the theory of references 6 and 8 would underpredict the flight data by at most 5 percent over the entire data acquisition period for which turbulent data were obtained. This result suggests that a better value for the Reynolds analogy factor would be 1.1 for applying the theory of references 6 and 8 to high-speed flight.

The integral theory of references 6 and 8 was used to predict the heating rates in the transition region. At the beginning of transition the theoretical predictions were matched to the flight data. This matching procedure was used because of the large discrepancy between the data and the tangent-cone laminar predictions. The matching was done by calculating a Stanton number from the measured heating rates and the local stream condition computed from the laminar tangent-cone theory. A Reynolds analogy

factor of 1.0 was then used to obtain an initial value for the skin friction coefficient. All other initial quantities were obtained from solutions of the laminar-boundary-layer equations. Application of this matching method gave good prediction for the trends in the heating rates in the transition region (fig. 2). The absolute magnitudes of the predicted heating rates are in good agreement with the data at $h = 27.43$ and 21.34 km (90 000 and 70 000 ft); however, the predictions and data disagree by as much as 50 percent for one data point in the transition region at $h = 24.38$, 22.86, and 18.29 km (80 000, 75 000, and 60 000 ft). In view of the complexity of the flow in the transition region, these results are considered satisfactory.

RESULTS AND DISCUSSION OF WIND-TUNNEL TESTS

Turbulent Data

The turbulent heating results are presented in figures 3 and 4 for the leeward and windward rays. In figure 3 the turbulent heating rates at angle of attack for models with the 2.54-mm-radius (0.100 in.) smooth nose and the 2.44-mm-radius (0.096 in.) Reentry F nose were divided by the measured turbulent heating rate for the model with the 2.54-mm-radius (0.100 in.) smooth nose at zero angle of attack. The reference turbulent heating rates for models with the sharp nose and the 0.508-mm-radius (0.020 in.) nose were their respective measured turbulent values at zero angle of attack. The data at the various angles of attack were obtained during different wind-tunnel tests; therefore, the total pressure and temperature and the wall temperature were, in general, somewhat different for the various tests. Correction factors for the heating-rate ratios were derived to account for these differences by using the Blasius skin-friction equation and Colburn's Reynolds analogy factor with the reference temperature expressions of reference 20. The derivation is given in the appendix.

The heat-transfer distribution indicated that little turbulent flow occurred on the models with the large nose radii (2.54 and 2.44 mm or 0.10 and 0.096 in.). Hence, it is not certain that a fully developed turbulent boundary layer existed on the models with these nose radii. Turbulent data were available over a greater length of the models when the smaller nose radii $(r_n = 0$ and 0.508 mm or 0.020 in.$)$ were used.

Curves were faired through the heating-rate-ratio data and the ratios for the largest s values (figs. 3(a) to (d)) or the faired asymptotic values (figs. 3(e) to (g)) were plotted against angle of attack for the windward and leeward rays in figure 4. As noted previously, the small-nose-radius data probably represent the better variation of the heating-rate ratio for the fully developed turbulent flow with angle of attack than the large-nose-radius data. Hence, a curve was fitted to the small-nose-radius data and the following relationship was obtained:

$$\frac{q_\alpha}{q_{\alpha=0}} = 1 - 0.1333\alpha \cos \phi \tag{1}$$

The theoretical equations used in references 4 and 5 to correct the heat-transfer data for angle of attack and azimuthal angle can be expressed as

$$\frac{q_\alpha}{q_{\alpha=0}} = 1 - 0.25\alpha \cos \phi \tag{2}$$

Therefore, the present results show much less effect of angle of attack on turbulent heating than the theoretical values used in references 4 and 5.

It was noted in reference 5, however, that the turbulent heating-rate ratio for the Reentry F flight data could be represented as follows:

$$\frac{q_\alpha}{q_{\alpha=0}} = 1 - 0.15\alpha \cos \phi \tag{3}$$

This result is in close agreement with the present wind-tunnel results given by equation (1).

For small nose radii, a 10^o roll had a negligible effect on the turbulent-heating-rate ratio (fig. 4). There appears to be some influence of roll on the heating-rate ratio for the Reentry F model nose but, because of the limited amount of turbulent data, this evidence is inconclusive.

The wind-tunnel tests, conducted with various noses over a limited angle-of-attack range, show that for fully developed turbulent flow, the Reentry F nose geometry and a 10^o roll do not significantly influence the rate of heat transfer to the windward and leeward rays of the Reentry F vehicle. Also, the wind-tunnel data and the results of reference 5 show that the influence of angle of attack should not exceed ±10 percent since the local angle of attack in the turbulent-flow region never exceeded 0.8^o.

Laminar Data

The laminar heating-rate results obtained from the wind-tunnel investigation are presented in ratio form in figure 5. The laminar heating rates at angle of attack for the models with the 2.54-mm-radius (0.10 in.) smooth nose and the 2.44-mm-radius (0.096 in.) Reentry F nose were divided by the measured laminar heating rate for the model with the 2.54-mm-radius (0.10 in.) smooth nose at zero angle of attack. The reference laminar heating rates for models with the sharp nose and the 0.508-mm-radius (0.020 in.) nose were the respective measured laminar values at zero angle of attack. The heating-rate ratios were corrected for differences in total pressure and temperature

and wall temperature by using the results of reference 21. The derivation of the correction factor is given in the appendix. Although considerable scatter exists in the corrected data, it is believed that meaningful trends can be obtained from the data.

Figure 5(a) shows that, at angle of attack, there is a large variation of the heating-rate ratio along the sharp cone on the leeward ray. This variation was unexpected since it is usually assumed that $q \propto \frac{1}{\sqrt{R_s}}$ along conical rays at angle of attack (ref. 18) and, when the data are presented in the form of $q_\alpha/q_{\alpha=0}$, the effect of Reynolds number would cancel. A limited test was conducted with a 10° half-angle cone, which had better instrumentation than the 5° half-angle conical model, to further investigate this variation. These results are discussed subsequently.

The sharp-cone data of figure 5(a) are plotted as a function of angle of attack for the windward and leeward rays in figure 6. The bars represent the maximum variation of the laminar heating rates, and the symbols represent the value of the heating rate obtained from a fairing of the data from figure 5(a) $(\phi = 0, \quad r_n = 0)$ at the largest values of s. The Reentry F flight data are also plotted in figure 6. The zero-angle-of-attack heating rates used to nondimensionalize the flight data were obtained from theoretical calculations based on the methods of references 6 and 7. The angles of attack for the flight data include the estimated effect of local thermal deformation. The Reentry F data correlate well in this figure.

In general, the wind-tunnel data for the most leeward ray of the sharp cone varied from the tangent-cone theoretical value near the nose to values substantially below those from the theory as distance from the nose increased. The sharp-cone data were above the Reentry F data on the leeward ray for angles of attack above 0.5°. On the leeward ray the linearized sharp-cone-theory predictions (ref. 18) in figure 6 have about the same slope with angle of attack as the wind-tunnel data (open circular symbols) but are somewhat below the data. The linearized theoretical predictions also agree with the Reentry F data for angles of attack up to about 0.8°. However, the linearized theory does not agree with the wind-tunnel data on the windward ray above 0.5° angle of attack.

The laminar-heating-rate data for the 2.54-mm-radius (0.10 in.) nose (fig. 5(b)) are presented in figure 7 as a function of angle of attack. A comparison of the results in figures 6 and 7 indicates that blunting the nose of the 5° half-angle cone resulted in some reduction of the downstream asymptotic value of the heating-rate ratio. The wind-tunnel data shown in figure 7 agree well with the Reentry F data up to an angle of attack of about 1.0°.

The wind-tunnel data for the Reentry F nose (figs. 5(c) to (f)) are presented in figure 8 which shows the effect of nose radius and roll. The 2.44-mm-radius (0.096 in.) Reentry F (fig. 8(a)) nose reduced the asymptotic values of the heating-rate ratio slightly below the value for the smooth model with a 2.54-mm (0.10 in.) nose radius (fig. 7) on

the leeward ray at 1.5° angle of attack. On the windward ray the influence of the Reentry F nose was also small and tended to increase slightly the heating-rate ratio above the values for the smooth model. The effect of a 10° roll was negligible in the angle-of-attack range of the investigation.

In figures 6, 7, and 8 the wind-tunnel data for the leeward ray were above the corresponding Reentry F data for angles of attack greater than about 0.8°. Also, on the leeward surface the predictions from the linear theory for wind-tunnel conditions $(t_w = 0.4, M_\infty = 8)$ were above the flight data for flight conditions $(t_w = 0.05, M_\infty = 20)$. (See figs. 6 and 8(a).) These differences are apparently due to the different Mach numbers and values of t_w. If the predicted differences are used to correct the wind-tunnel data to flight conditions, there would be good agreement between the flight and wind-tunnel data for the angle-of-attack range of the investigation. The major discrepancy between the flight data and the corrected theoretical predictions occurred near zero angle of attack (high altitudes) where the heating rates are low and the flight measurements have the greater relative error.

The heating rates measured on the model using the nose with the forward-facing step that simulates a flank failure of the graphite nose section are presented in ratio form in figures 5(g) and 8(c). This configuration resulted in some reduction in the heating-rate ratio when compared with the ratios for the Reentry F nose $(r_n = 2.44$ mm (0.096 in.)). These wind-tunnel data, obtained with the forward-facing step, also agree with the flight data. However, if these wind-tunnel data were corrected for the effects of Mach number and t_w (as noted previously), the wind-tunnel data would be below the flight data. This method of correcting the wind-tunnel data for Mach number and t_w effects suggests that the wind-tunnel data obtained with the Reentry F nose represent a good approximation of the rate of heat transfer to the flight vehicle. Furthermore, the assumption of a failure of the flight nose section does not improve the agreement between flight data and predictions.

The results discussed thus far indicate that the tangent-cone method is inadequate for predicting laminar heating rates on the most leeward ray of slender cones at small angles of attack. A linear theory for sharp cones at angle of attack was shown to predict both the wind-tunnel and flight data for the leeward ray to fair accuracy. A more complete system of equations is needed to accurately predict the laminar heating rates on slender cones at angles of attack. These equations should use the results of nonlinear inviscid flow-field calculations for boundary-layer edge conditions (ref. 22) and the boundary-layer equations should include the effect of cross flow in the boundary layer (ref. 23).

From the results of linear theory and wind-tunnel tests, the low laminar heating rates measured on the Reentry F flight vehicle and described in references 4 and 5 have been explained. The observed reduction in the heating rates was due to an increase in the local angle of attack with a decrease in altitude (where the local angle of attack consists

of the sum of the mean angle of attack of the body plus that due to local body bending caused by thermal distortion). Nose bluntness causes some reduction in heating; however, this reduction is small when compared with the reduction due to angle of attack.

As noted previously, results in figure 5(a) of the laminar tests with the sharp 5° half-angle cone at angle of attack indicated a large axial variation of the heating-rate ratio on the leeward ray of the model. A test was conducted with a 10° half-angle cone to further investigate this axial variation. The results of the experiment with this model are shown in figure 9. These results show a similar variation of the heating-rate ratio with surface distance at the highest angle of attack on the leeward ray as found with the 5° half-angle cone (fig. 5(a)). This variation also disagrees with the usual assumption that $q \propto \frac{1}{\sqrt{R_s}}$ along the rays of a cone at angle of attack. The observed difference between the variations of theoretical and measured heating-rate ratios with distance on the lee side is believed to be associated with the partial failure of the boundary-layer equations near the tip of the cone; that is, some finite distance may be required to reach predicted values of boundary-layer thickness on the lee side of the cone.

CONCLUSIONS

The laminar, transitional, and turbulent heat-transfer rates measured on the main thermocouple ray for the Reentry F flight experiment over a range of altitude from 36.58 to 18.29 km (120 000 to 60 000 ft) have been compared with predictions from laminar and turbulent theories and with wind-tunnel results. The major conclusions from these comparisons are as follows:

1. Measured turbulent heating rates and the predictions from an integral-type turbulent theory agreed to within 10 to 20 percent over the altitude range where the boundary layer was turbulent (27.43 to 18.29 km or 90 000 to 60 000 ft). The prediction methods assumed a Reynolds analogy factor of 1.0. With the assumed Reynolds analogy factor increased to 1.1, the theory underpredicted the data by at most 5 percent.

2. The laminar tangent-cone method, with flow assumed along rays, predicted the laminar lee-side data to within 20 percent at altitudes from 36.58 to 24.38 km (120 000 to 80 000 ft) and mean trim angle of attack less than 0.15°. At lower altitudes and a mean trim angle of attack greater than 0.4°, the data were substantially below the laminar predictions. At 18.29 km (60 000 ft), the data were only 40 percent of the predictions at the most forward thermocouple station (effective angle of attack of 1.55°).

Therefore, the laminar tangent-cone theory does not provide reliable predictions for leeward heating on slender cones (cone half-angle equal to 5°) at angles of attack greater than a few tenths of a degree.

3. Heating-rate predictions from linearized laminar theory for sharp cones at angle of attack were in fair agreement with measured laminar heating rates on the main thermocouple ray over an altitude range from 36.58 to 18.29 km (120 000 to 60 000 ft).

Langley Research Center,
National Aeronautics and Space Administration,
Hampton, Va., June 5, 1972.

APPENDIX

CORRECTION FACTORS FOR HEATING-RATE RATIOS

Symbols

The symbols in this section are used only in the calculations presented in the appendix. The symbols used and defined in the text are not redefined herein.

c_f local skin-friction coefficient

c_p specific heat at constant pressure

H local total enthalpy in boundary layer

H_e free-stream total enthalpy

M Mach number

N_{Pr} Prandlt number

N_{St} Stanton number, $\frac{h}{\rho u c_p}$ where $h = \frac{q}{T_{aw} - T_w}$

n exponent of Reynolds number in Blasius skin-friction equation

p pressure

R_e Reynolds number based on local edge properties

T temperature

u velocity in s-direction

γ ratio of specific heats

$\zeta = \frac{H}{H_e}$

μ coefficient of viscosity

ρ density

APPENDIX

Subscripts:

aw	adiabatic wall
e	boundary-layer local edge
t	total
w	wall
1	a given tunnel test condition
2	a tunnel test condition in the neighborhood of given condition 1
∞	free stream

An asterisk with a symbol indicates quantity evaluated at reference temperature of reference 20.

A prime with a symbol denotes differentiation with respect to η, the similarity parameter of reference 21.

Derivation of Equations

The wind-tunnel heat-transfer data have been presented in the form of heating-rate ratios. Since the data for the various angles of attack were obtained during different wind-tunnel runs, the total pressure and temperature and wall temperature differed, in general, by small amounts for the various runs. Thus, the heating-rate ratio must be corrected to account for these differences. The laminar heating-rate ratios were corrected by using the results of reference 21; the turbulent rates were corrected by using the Blasius skin-friction equation and Colburn's Reynolds analogy factor with the reference temperature expressions of reference 20.

The basic heating-rate-ratio correction formulation is as follows:

$$\left(\frac{q_{\alpha,1}}{q_{\alpha=0,1}}\right)_{\text{corrected}} = \frac{q_{\alpha,1}}{q_{\alpha=0,2}} \frac{q_{\alpha=0,2}}{q_{\alpha=0,1}} \tag{A1}$$

where subscript 1 represents a given tunnel test condition and subscript 2 represents another condition in the neighborhood of the given condition. By using the definitions of the heat-transfer coefficient and the Stanton number, the correction factor $\frac{q_{\alpha=0,2}}{q_{\alpha=0,1}}$ can be expressed as

APPENDIX

$$\frac{q_{\alpha=0,2}}{q_{\alpha=0,1}} = \frac{N_{St,2}(\rho u c_p)_2 (T_{aw} - T_w)_2}{N_{St,1}(\rho u c_p)_1 (T_{aw} - T_w)_1} \tag{A2}$$

An expression for N_{St} can be obtained from reference 20 by using the Blasius skin-friction equation $\left(c_f \propto \frac{1}{(R_e)^n}\right.$ where for laminar boundary layers $n = 0.5$ and for turbulent boundary layers $\left. n = 0.2\right)$ and Colburn's Reynolds analogy factor. Thus,

$$\frac{q_{\alpha=0,2}}{q_{\alpha=0,1}} = \frac{(R^*_{e,1})^n}{(R^*_{e,2})^n} \left(\frac{N^*_{Pr,1}}{N^*_{Pr,2}}\right)^{2/3} \frac{\rho^*_2 u_{e,2} c^*_{p,2}}{\rho^*_1 u_{e,1} c^*_{p,1}} \frac{(T_{aw} - T_w)_2}{(T_{aw} - T_w)_1} \tag{A3}$$

where the reference (*) conditions refer to

$$\frac{T^*}{T_t} = \frac{T_e}{T_t} + 0.5\left(\frac{T_w}{T_t} - \frac{T_e}{T_t}\right) + 0.22\left(\frac{T_{aw}}{T_t} - \frac{T_e}{T_t}\right) \tag{A4}$$

and

$$\frac{T_e}{T_t} = \frac{T_e}{T_\infty} \frac{T_\infty}{T_t}$$

$$\frac{T_{aw}}{T_t} = r\left(1 - \frac{T_e}{T_t}\right) + \frac{T_e}{T_t}$$

$r = \sqrt{N_{Pr}}$ for laminar flow

$r = \sqrt[3]{N_{Pr}}$ for turbulent flow

$$\frac{T_t}{T_\infty} = 1 + \frac{\gamma - 1}{2} M^2_\infty$$

The values for T_e/T_∞ are obtained from cone or wedge conditions. By using the definition of Reynolds number, equation (A3) can be expressed in general terms to give

APPENDIX

$$\frac{q_{\alpha=0,2}}{q_{\alpha=0,1}} = \left(\frac{p_{t,2}}{p_{t,1}}\right)^{1-n}\left(\frac{M_{e,2}}{M_{e,1}}\right)^{1-n}\left(\frac{s_1}{s_2}\right)^{n}\left(\frac{N^*_{Pr,1}}{N^*_{Pr,2}}\right)^{\frac{2}{3}}\left(\frac{c^*_{p,2}}{c^*_{p,1}}\right)\left(\frac{T_{t,2}}{T_{t,1}}\right)^{\frac{1+2n}{2}}\left[\left(\frac{\frac{T^*_2}{T_{t,2}}}{\frac{T^*_1}{T_{t,1}}}\right)^{\frac{3}{2}}\left(\frac{\frac{T^*_1}{T_{t,1}}+\frac{200}{T_{t,1}}}{\frac{T^*_2}{T_{t,2}}+\frac{200}{T_{t,2}}}\right)^{n}\right]$$

$$\times\left(\frac{\frac{p_{\infty,2}}{p_{t,2}}\frac{p_{e,2}}{p_{\infty,2}}}{\frac{p_{\infty,1}}{p_{t,1}}\frac{p_{e,1}}{p_{\infty,1}}}\right)^{1-n}\left(\frac{\frac{T^*_{e,1}}{T_{t,1}}}{\frac{T^*_{e,2}}{T_{t,2}}}\right)\left(\frac{\frac{T_{\infty,2}}{T_{t,2}}\frac{T_{e,2}}{T_{\infty,2}}}{\frac{T_{\infty,1}}{T_{t,1}}\frac{T_{e,1}}{T_{\infty,1}}}\right)^{\frac{1-n}{2}}\frac{\left(\frac{T_{aw}}{T_t}-\frac{T_w}{T_t}\right)_2}{\left(\frac{T_{aw}}{T_t}-\frac{T_w}{T_t}\right)_1} \tag{A5}$$

If wind-tunnel conditions 1 and 2 are not too different, equation (A5) can be simplified to give

$$\frac{q_{\alpha=0,2}}{q_{\alpha=0,1}} = \left(\frac{p_{t,2}}{p_{t,1}}\right)^{1-n}\left(\frac{T_{t,2}}{T_{t,1}}\right)^{\frac{1+2n}{2}}\left(\frac{\frac{T^*_1}{T_{t,1}}+\frac{200}{T_{t,1}}}{\frac{T^*_2}{T_{t,2}}+\frac{200}{T_{t,2}}}\right)^{n}\left(\frac{\frac{T^*_1}{T_{t,1}}}{\frac{T^*_2}{T_{t,2}}}\right)^{-\left(\frac{5n-2}{2}\right)}\frac{\left(\frac{T_{aw}-T_w}{T_t}\right)_2}{\left(\frac{T_{aw}-T_w}{T_t}\right)_1} \tag{A6}$$

The foregoing reductions assume that $M_{\infty,1} = M_{\infty,2}$, N_{Pr}, and c_p are constants, and $s_2 \approx s_1$. Equation (A6) thus becomes for a turbulent boundary layer where $n = 0.2$

$$\frac{q_{\alpha=0,2}}{q_{\alpha=0,1}} = \left(\frac{p_{t,2}}{p_{t,1}}\right)^{0.8}\left(\frac{T_{t,2}}{T_{t,1}}\right)^{0.7}\left(\frac{\frac{T^*_1}{T_{t,1}}+\frac{200}{T_{t,1}}}{\frac{T^*_2}{T_{t,2}}+\frac{200}{T_{t,2}}}\right)^{0.2}\left(\frac{\frac{T^*_1}{T_{t,1}}}{\frac{T^*_2}{T_{t,2}}}\right)^{0.5}\frac{\left(\frac{T_{aw}-T_w}{T_t}\right)_2}{\left(\frac{T_{aw}-T_w}{T_t}\right)_1} \tag{A7}$$

or for a laminar boundary layer where $n = 0.5$

$$\frac{q_{\alpha=0,2}}{q_{\alpha=0,1}} = \left(\frac{p_{t,2}}{p_{t,1}}\right)^{0.5}\left(\frac{T_{t,2}}{T_{t,1}}\right)^{1.0}\left(\frac{\frac{T^*_1}{T_{t,1}}+\frac{200}{T_{t,1}}}{\frac{T^*_2}{T_{t,2}}+\frac{200}{T_{t,2}}}\right)^{0.5}\left(\frac{\frac{T^*_1}{T_{t,1}}}{\frac{T^*_2}{T_{t,2}}}\right)^{-0.25}\frac{\left(\frac{T_{aw}-T_w}{T_t}\right)_2}{\left(\frac{T_{aw}-T_w}{T_t}\right)_1} \tag{A8}$$

APPENDIX

A second correction factor for the laminar boundary layer can be obtained for equation (A1) by using the results of reference 21. From this reference it can be shown that the rate of heat transfer to a cone is given by

$$q = \sqrt{\frac{3}{2}} \frac{H_e \zeta'_w}{N_{Pr,w}} \sqrt{\frac{\rho_w \mu_w u_e}{s}} \tag{A9}$$

Equation (A9) is expressed in ratio form as

$$\frac{q_{\alpha=0,2}}{q_{\alpha=0,1}} = \left(\frac{H_{e,2}}{H_{e,1}}\right)\left(\frac{\zeta'_{w,2}}{\zeta'_{w,1}}\right)\left(\frac{\rho_{w,2}}{\rho_{w,1}}\right)^{\frac{1}{2}}\left(\frac{\mu_{w,2}}{\mu_{w,1}}\right)^{\frac{1}{2}}\left(\frac{u_{e,2}}{u_{e,1}}\right)^{\frac{1}{2}}\left(\frac{s_1}{s_2}\right)^{\frac{1}{2}} \frac{(N_{Pr,w})_1}{(N_{Pr,w})_2} \tag{A10}$$

Equation (A10) can be put in the form of measured and tabulated quantities as follows:

$$\frac{q_{\alpha=0,2}}{q_{\alpha=0,1}} = \left(\frac{T_{t,2}}{T_{t,1}}\right)\left(\frac{p_{t,2}}{p_{t,1}}\right)^{\frac{1}{2}}\left(\frac{M_{e,2}}{M_{e,1}}\right)^{\frac{1}{2}}\left(\frac{\zeta'_{w,2}}{\zeta'_{w,1}}\right)\frac{(N_{Pr,w})_1}{(N_{Pr,w})_2}\left(\frac{p_{e,2}}{p_{\infty,2}}\frac{p_{\infty,2}}{p_{t,2}}\frac{p_{\infty,1}}{p_{e,1}}\frac{p_{t,1}}{p_{\infty,1}}\right)^{\frac{1}{2}}$$

$$\times\left(\frac{T_{w,2}}{T_{t,2}}\frac{T_{t,1}}{T_{w,1}}\right)^{\frac{1}{4}}\left(\frac{T_{e,2}}{T_{\infty,2}}\frac{T_{\infty,2}}{T_{t,2}}\frac{T_{\infty,1}}{T_{e,1}}\frac{T_{t,1}}{T_{\infty,1}}\right)^{\frac{1}{4}}\left[\frac{\left(\frac{T_w}{T_t}+\frac{200}{T_t}\right)_1}{\left(\frac{T_w}{T_t}+\frac{200}{T_t}\right)_2}\right]^{\frac{1}{2}} \tag{A11}$$

Again, if wind-tunnel conditions 1 and 2 are not too different, equation (A11) can be expressed as

$$\frac{q_{\alpha=0,2}}{q_{\alpha=0,1}} = \left(\frac{T_{t,2}}{T_{t,1}}\right)\left(\frac{p_{t,2}}{p_{t,1}}\right)^{\frac{1}{2}}\left(\frac{\zeta'_{w,2}}{\zeta'_{w,1}}\right)\left(\frac{T_{w,2}}{T_{t,2}}\frac{T_{t,1}}{T_{w,1}}\right)^{\frac{1}{4}}\left[\frac{\left(\frac{T_w}{T_t}+\frac{200}{T_t}\right)_1}{\left(\frac{T_w}{T_t}+\frac{200}{T_t}\right)_2}\right]^{\frac{1}{2}} \tag{A12}$$

Equation (A12) was used in the present report to correct the measured laminar heating-rate ratios. The quantity ζ'_w was predominantly a function of T_w/T_t. Therefore, values of ζ'_w were obtained from a curve fitted to similar solutions (ref. 21) of the boundary-layer equation for the present tunnel conditions.

REFERENCES

1. Kline, S. J.; Morkovin, M. V.; Sovran, G.; and Cockrell, D. J., eds.: Computation of Turbulent Boundary Layers – 1968 AFOSR-IFR-Stanford Conference. Vol. I – Methods, Predictions, Evaluation and Flow Structure. Stanford Univ., c.1969.
   Coles, D. E.; and Hirst, E. A., eds.: Computation of Turbulent Boundary Layers – 1968 AFOSR-IFP-Stanford Conference. Vol. II – Compiled Data. Stanford Univ., c.1969.

2. Anon.: Compressible Turbulent Boundary Layers. NASA SP-216, 1969.

3. Beckwith, Ivan E.: Recent Advances in Research on Compressible Turbulent Boundary Layers. Analytic Methods in Aircraft Aerodynamics, NASA SP-228, 1970, pp. 355-416.

4. Rumsey, Charles B.; Carter, Howard S.; Hastings, Earl C., Jr.; Raper, James L.; and Zoby, Ernest B.: Initial Results From Flight Measurements of Turbulent Heat Transfer and Boundary-Layer Transition at Local Mach Numbers Near 15 (Reentry F). NASA TM X-1856, 1969.

5. Zoby, Ernest V.; and Rumsey, Charles B.: Analysis of Free-Flight Laminar, Transitional, and Turbulent Heat-Transfer Results at Free-Stream Mach Numbers Near 20 (Reentry F). NASA TM X-2335, 1971.

6. Johnson, Charles B.; Stainback, P. Calvin; Wicker, Kathleen C.; and Boney, Lillian R.: Boundary-Layer Edge Conditions and Transition Reynolds Number Data for a Flight Test at Mach 20 (Reentry F). NASA TM X-2584, 1972.

7. Stainback, P. Calvin (With appendix by P. Calvin Stainback and Kathleen C. Wicker): Effect of Unit Reynolds Number, Nose Bluntness, Angle of Attack, and Roughness on Transition on a 5° Half-Angle Cone at Mach 8. NASA TN D-4961, 1969.

8. Johnson, Charles B.; and Boney, Lillian R.: A Simple Integral Method for the Calculation of Real-Gas Turbulent Boundary Layers With Variable Edge Entropy. NASA TN D-6217, 1971.

9. Wright, Robert L.; and Zoby, Ernest V.: Flight Measurements of Boundary-Layer Transition on a 5° Half-Angle Cone at a Free-Stream Mach Number of 20 (Reentry F). NASA TM X-2253, 1971.

10. Carter, Howard S.; Raper, James L.; Hinson, William F.; and Morris, W. Douglas: Basic Measurements From a Turbulent-Heating Flight Experiment on a 5° Half-Angle Cone at Mach 20 (Reentry F). NASA TM X-2308, 1971.

11. Woodbury, Gerard E.; and Morris, W. Douglas: Angle-of-Attack Analysis of a Spinning Slender Cone With Slight Aerodynamic and Mass Asymmetries (Reentry F). NASA TN D-5948, 1970.

12. Dillon, James L.: Analysis of Surface Pressure on a 5° Cone in Free Flight Near Mach 20 (Reentry F). NASA TM X-2210, 1971.

13. Howard, Floyd G.: Thermal Analysis Methods and Basic Heat-Transfer Data for a Turbulent Heating Flight Experiment at Mach 20 (Reentry F). NASA TM X-2282, 1971.

14. Alley, Vernon L., Jr.; and Guillotte, Robert J.: Postflight Analysis of Thermal Distortions of the Reentry F Spacecraft. NASA TM X-2250, 1971.

15. Stainback, P. Calvin: Heat-Transfer Measurements at a Mach Number of 8 in the Vicinity of a 90° Interior Corner Alined With the Free-Stream Velocity. NASA TN D-2417, 1964.

16. Scheafer, William T., Jr.: Characteristics of Major Active Wind Tunnels at the Langley Research Center. NASA TM X-1130, 1965.

17. Stainback, P. Calvin: Heat-Transfer Measurements at a Mach Number of 4.95 on Two 60° Swept Delta Wings With Blunt Leading Edges and Dihedral Angles of 0° and 45°. NASA TN D-549, 1961.

18. Bodonyi, Richard J.; and Reshotko, Eli: The Compressible Laminar Boundary Layer With Heat Transfer on a Yawed Cone at Small Angle of Attack. FTAS/TR-70-48 (Contract No. NGL-36-003-064), Case Western Reserve Univ., Jan. 1970. (Available as NASA CR-109839.)

19. Cary, Aubrey M., Jr.: Summary of Available Information on Reynolds Analogy for Zero-Pressure-Gradient, Compressible, Turbulent-Boundary-Layer Flow. NASA TN D-5560, 1970.

20. Eckert, Ernst R. G.: Survey on Heat Transfer at High Speeds. ARL 189, U.S. Air Force, Dec. 1961. (Available from DDC as AD 274109.)

21. Cohen, Nathaniel B.: Boundary-Layer Similar Solutions and Correlation Equations for Laminar Heat-Transfer Distribution in Equilibrium Air at Velocities up to 41,000 Feet Per Second. NASA TR R-118, 1961.

22. Rakich, John V.: A Method of Characteristics for Steady Three-Dimensional Supersonic Flow With Application to Inclined Bodies of Revolution. NASA TN D-5341, 1969.

23. McGowan, J. J., III; and Davis, R. T.: Development of a Numerical Method To Solve the Three-Dimensional Compressible Laminar Boundary-Layer Equations With Application to Elliptical Cones at Angle of Attack. ARL 70-0341, U.S. Air Force, Dec. 1970.

TABLE I.- FLIGHT CONDITIONS FOR HEAT-TRANSFER CALCULATIONS USING TANGENT-CONE METHOD

h		V_∞		M_∞	r_n		α, deg (a)	α_{eff}, deg	$\theta_{c,eff}$, deg	$s_{t,b}$		$s_{t,e}$	
km	ft	km/sec	ft/sec		mm	in.				m	in.	m	in.
36.58	120 000	6.03	19 786	19.25	2.897	0.114	0	0	5	----	----	----	----
30.48	100 000	6.02	19 747	19.79	3.099	.122	0	0	5	2.908	114.5	----	----
27.43	90 000	6.00	19 687	20.07	3.251	.128	0	0	5	2.294	90.3	----	----
25.91	85 000	5.98	19 638	20.03	3.327	.131	0	0	5	2.169	85.4	3.424	134.8
24.38	80 000	5.96	19 572	19.97	3.430	.135	.140	.140	4.860	1.986	78.2	3.117	122.7
22.86	75 000	5.94	19 482	19.89	3.556	.140	.425	.425	4.575	1.402	55.2	2.629	103.5
21.34	70 000	5.90	19 367	19.95	3.683	.145	.660	.660	4.340	1.186	46.7	2.380	93.7
19.81	65 000	5.86	19 215	19.97	3.835	.151	.715	.715	4.285	.818	32.2	2.256	88.8
18.29	[b] 60 000	5.80	19 018	19.95	3.988	.157	.750	.750	4.250	.419	16.5	2.253	88.7
18.29	[c] 60 000	5.80	19 018	19.95	3.988	.157	.750	1.55	3.450	.419	16.5	2.253	88.7

[a] Since the angle of attack of the vehicle was less than 0.10^o for altitudes between 25.91 and 36.58 km (85 000 and 120 000 ft), the theoretical calculations were made for zero angle of attack. The effect of these small angles of attack on heating should be negligible.

[b] Condition assumed to be most applicable for turbulent portion of boundary layer.

[c] Conditions for station at $x = 40.6$ cm (16 in.) and assumed to be most applicable for laminar boundary layer at beginning of transition.

TABLE II.- LOCAL* EFFECTIVE ANGLE OF ATTACK OF CENTER LINE IN DEGREES FOR THERMOCOUPLES ON MAIN INSTRUMENTATION RAY

Altitude		α_{eff}, deg, of station at x, cm (in.), of –											
km	ft	40.6 (16)	78.7 (31)	101.6 (40)	132.1 (52)	150.6 (59.3)	185.4 (73)	215.9 (85)	251.5 (99)	276.9 (109)	307.3 (121)	337.8 (133)	365.8 (144)
36.58	120 000	0.08	0.08	0.08	0.08	0.08	0.08	0.08	0.08	0.08	0.08	0.08	0.08
30.48	100 000	.075	.075	.075	.075	.075	.075	.075	.075	.075	.075	.075	.075
27.43	90 000	.10	.10	.10	.10	.10	.10	.10	.10	.10	.10	.10	.10
25.91	85 000	-.08	-.04	-.039	-.048	-.052	-.057	-.0625	-.055	-.05	-.04	-.034	-.034
24.38	80 000	-.145	-.128	-.12	-.127	-.136	-.144	-.138	-.119	-.101	-.086	-.078	-.078
22.86	75 000	-.51	-.468	-.454	-.447	-.450	-.450	-.434	-.403	-.38	-.365	-.355	-.355
21.34	70 000	-.870	-.773	-.745	-.724	-.710	-.693	-.664	-.625	-.600	-.588	-.578	-.578
19.81	65 000	-1.160	-.96	-.907	-.855	-.824	-.773	-.730	-.680	-.700	-.641	-.633	-.629
18.29	60 000	-1.555	-1.190	-1.07	-.96	-.911	-.831	-.763	-.705	-.675	-.653	-.636	-.631

*Local effective angle of attack is equal to the sum of the distortion angle caused by thermal stresses and the mean trim angle of attack of the undistorted vehicle.

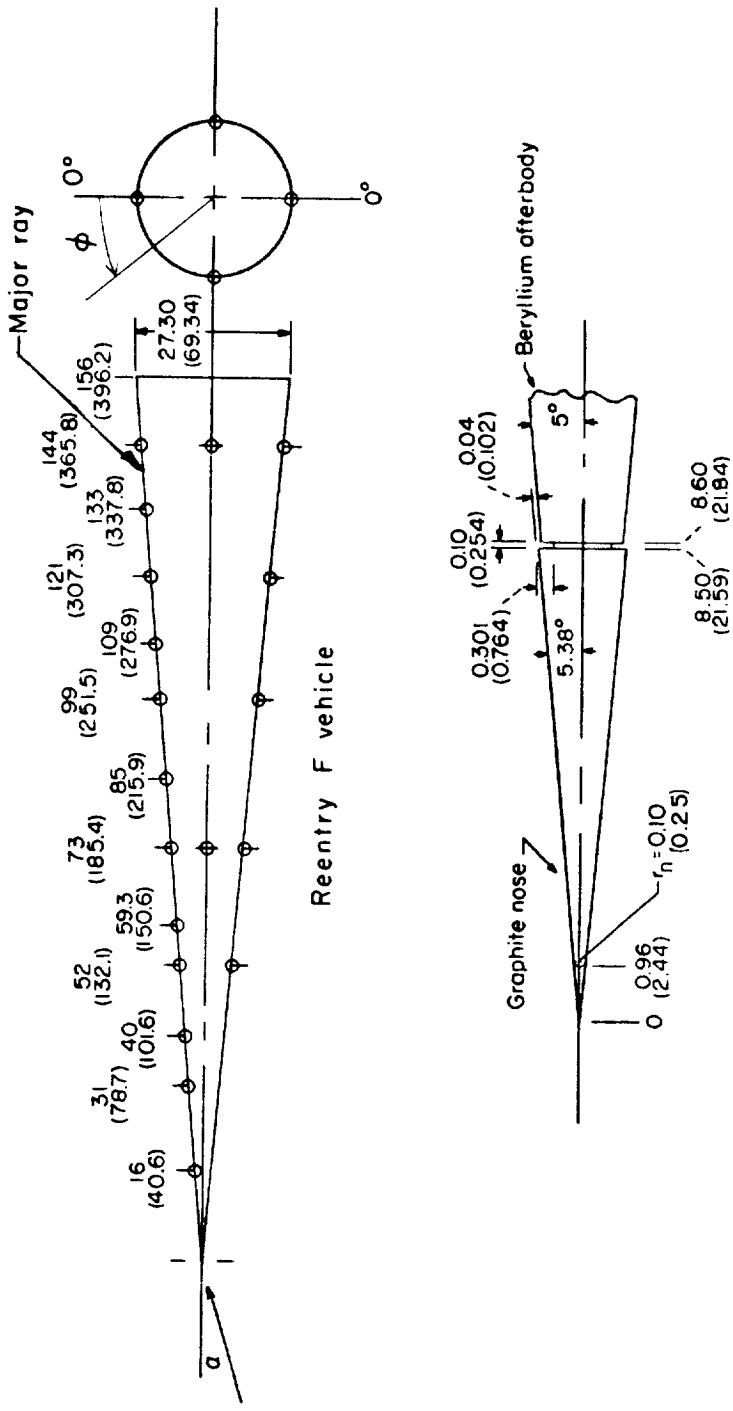

Figure 1.- Vehicle geometry and thermocouple locations. All dimensions are in inches (centimeters) and are for the preflight condition.

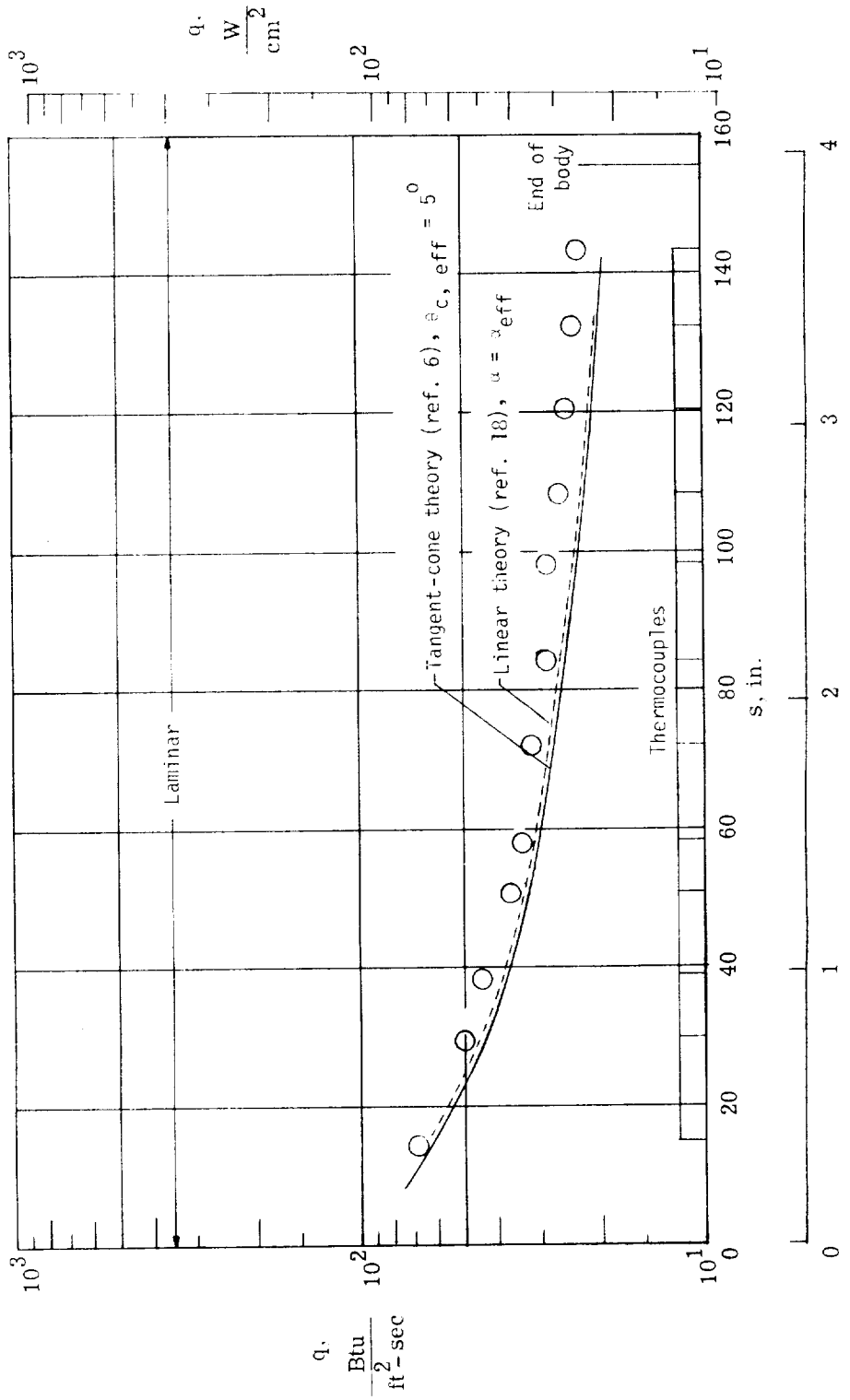

(a) h = 36.58 km (120 000 ft): V_∞ = 6.03 km/sec (19 786 ft/sec); r_n = 2.897 mm (0.114 in.).

Figure 2.- Rates of heat transfer to Reentry F vehicle. $\theta_s = 5^\circ$.

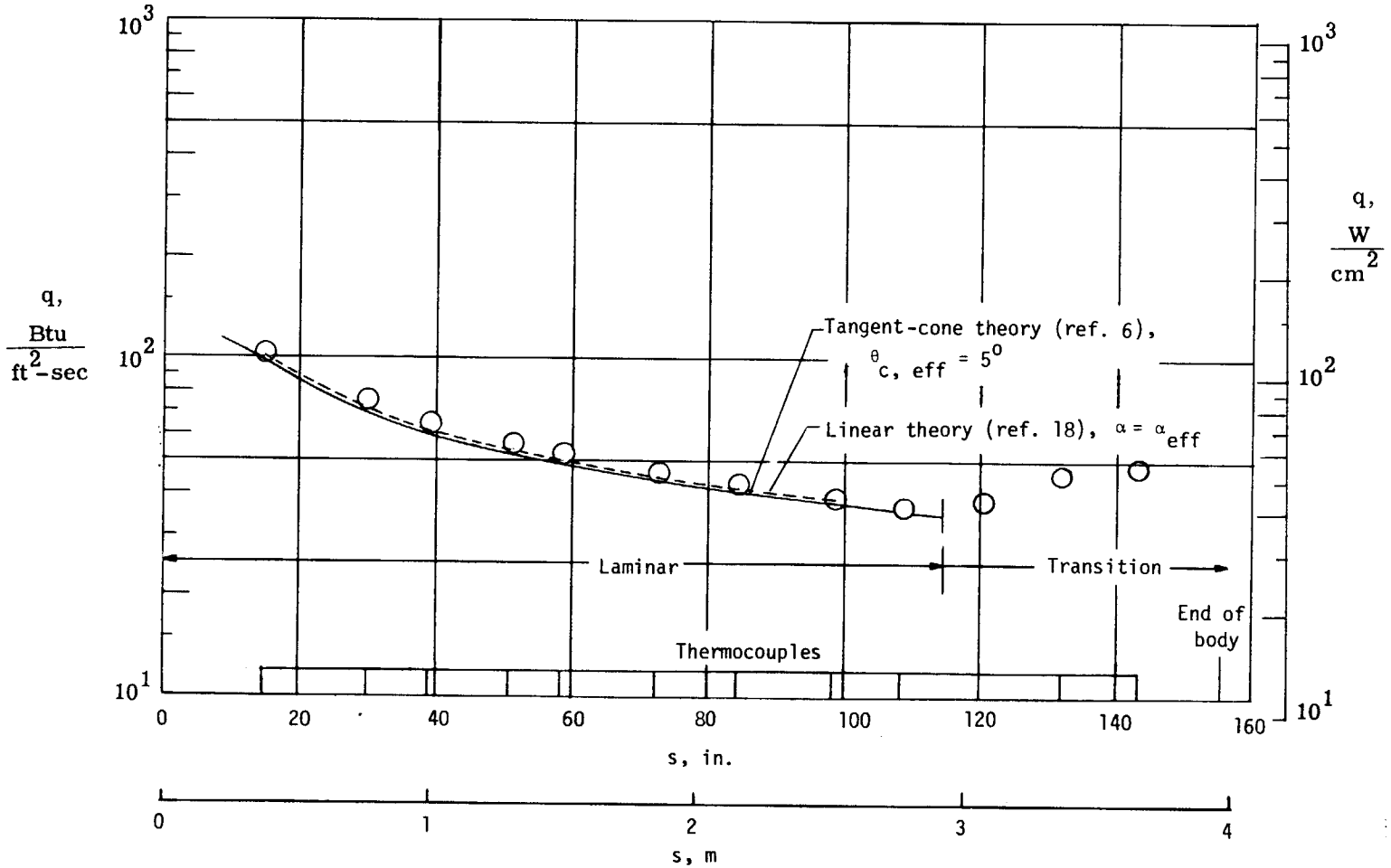

(b) h = 30.48 km (100 000 ft); V_∞ = 6.02 km/sec (19 747 ft/sec); r_n = 3.099 mm (0.122 in.).

Figure 2.- Continued.

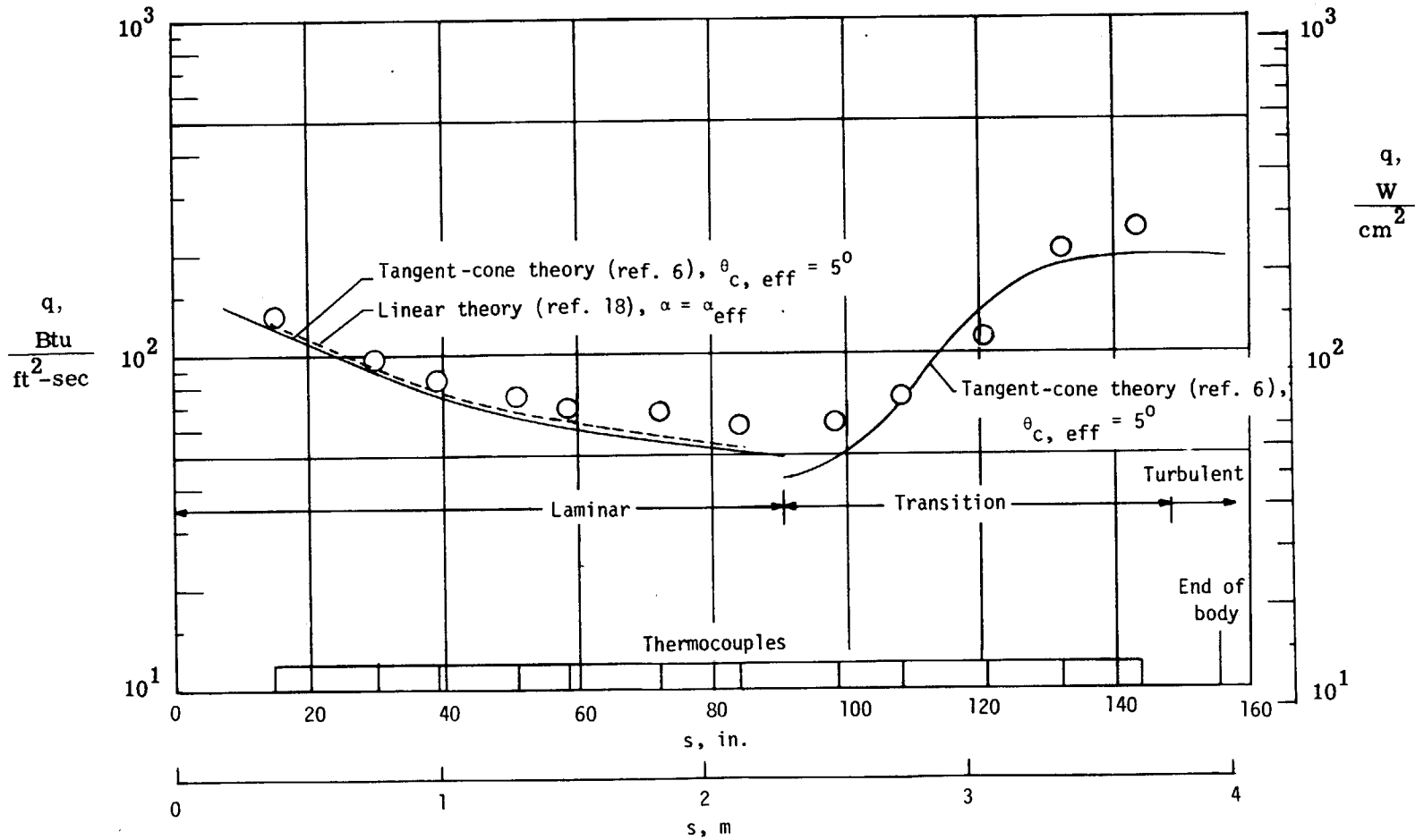

(c) h = 27.43 km (90 000 ft); V_∞ = 6.00 km/sec (19 687 ft/sec); r_n = 3.251 mm (0.128 in.).

Figure 2.- Continued.

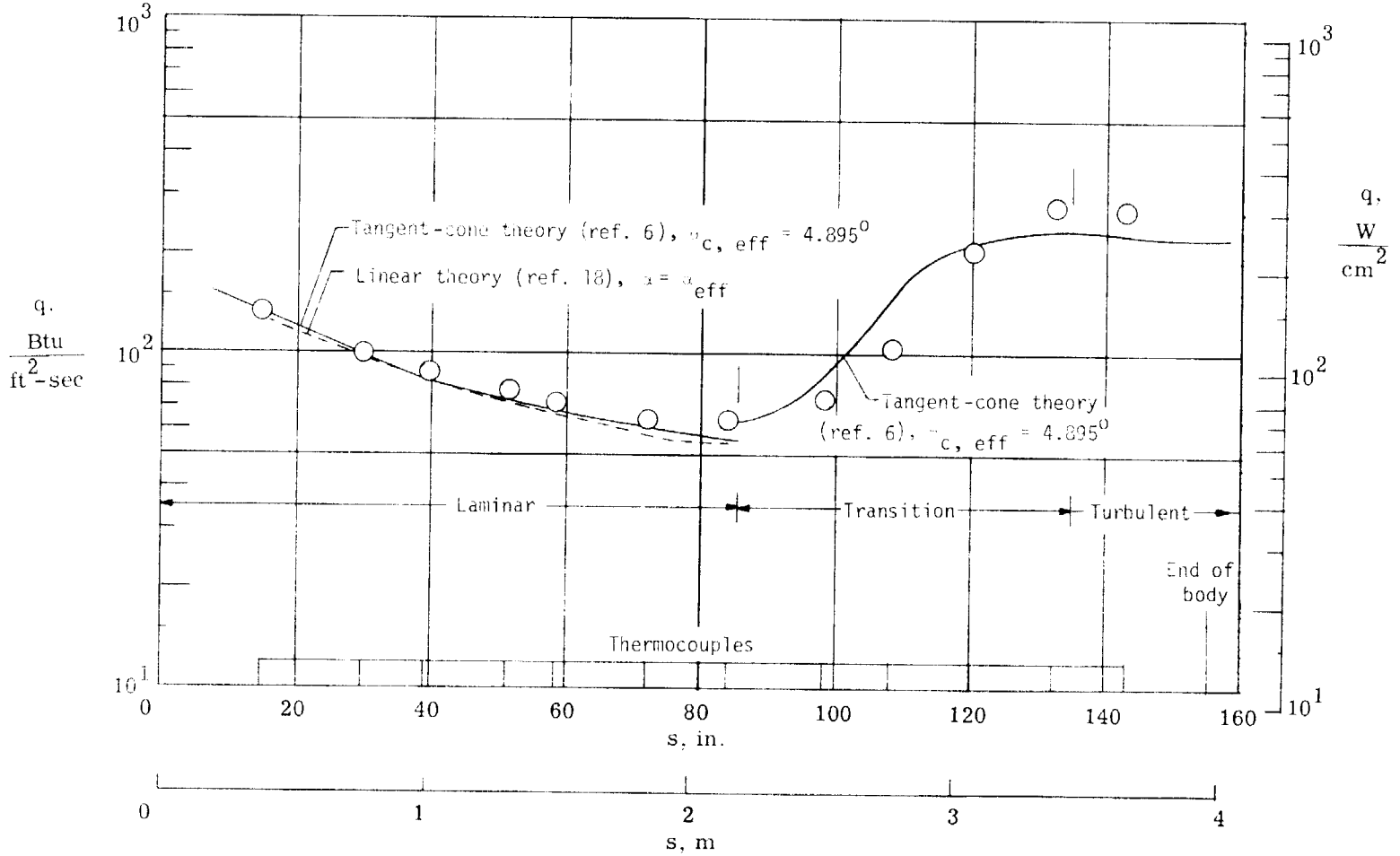

(d) h = 25.91 km (85 000 ft): V_∞ = 5.98 km/sec (19 638 ft/sec); r_n = 3.327 mm (0.131 in.).

Figure 2.- Continued.

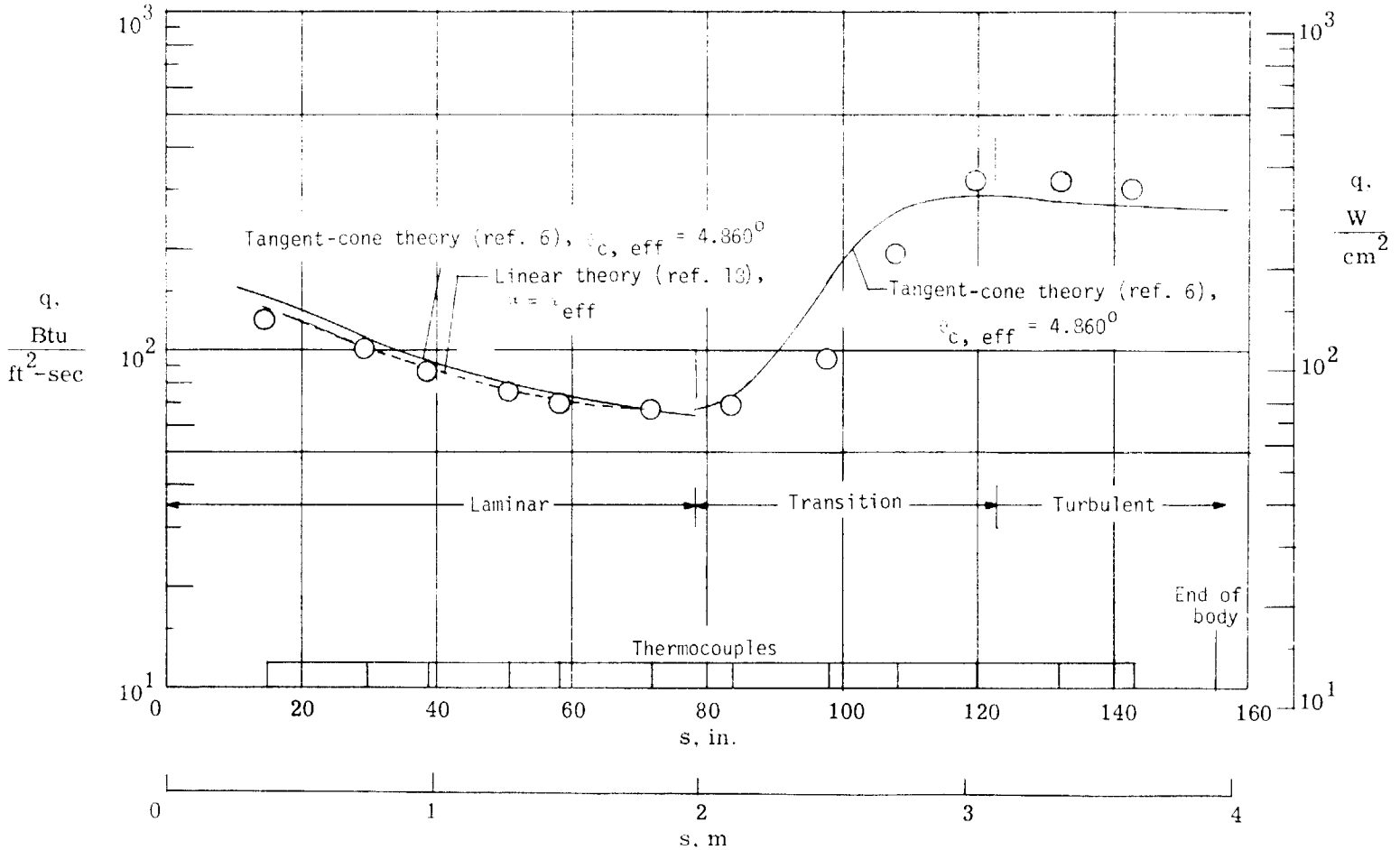

(e) h = 24.38 km (80 000 ft); V_∞ = 5.96 km/sec (19 572 ft/sec); r_n = 3.430 mm (0.135 in.).

Figure 2.- Continued.

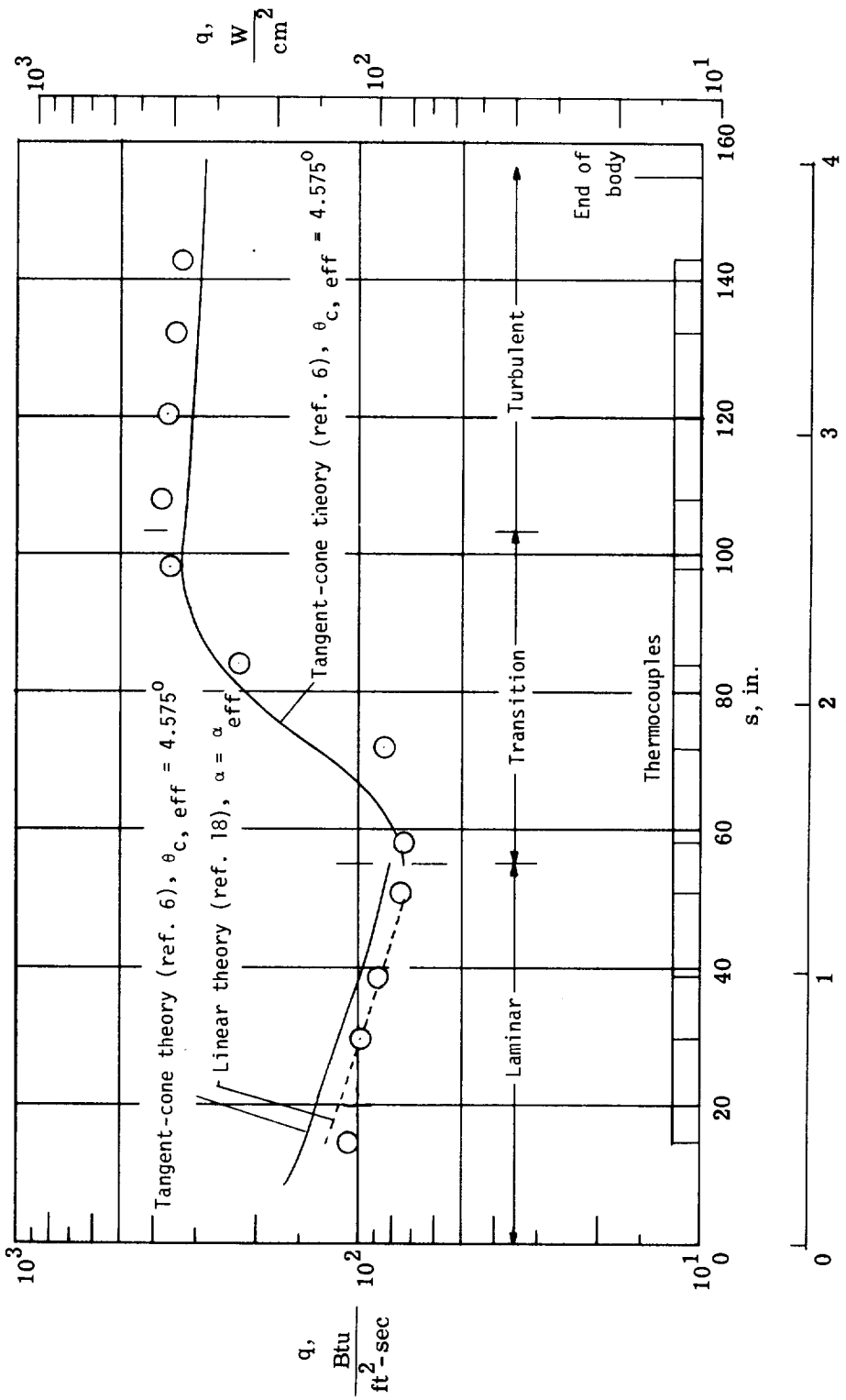

(f) h = 22.86 km (75 000 ft); V_∞ = 5.94 km/sec (19 482 ft/sec); r_n = 3.556 mm (0.140 in.).

Figure 2.- Continued.

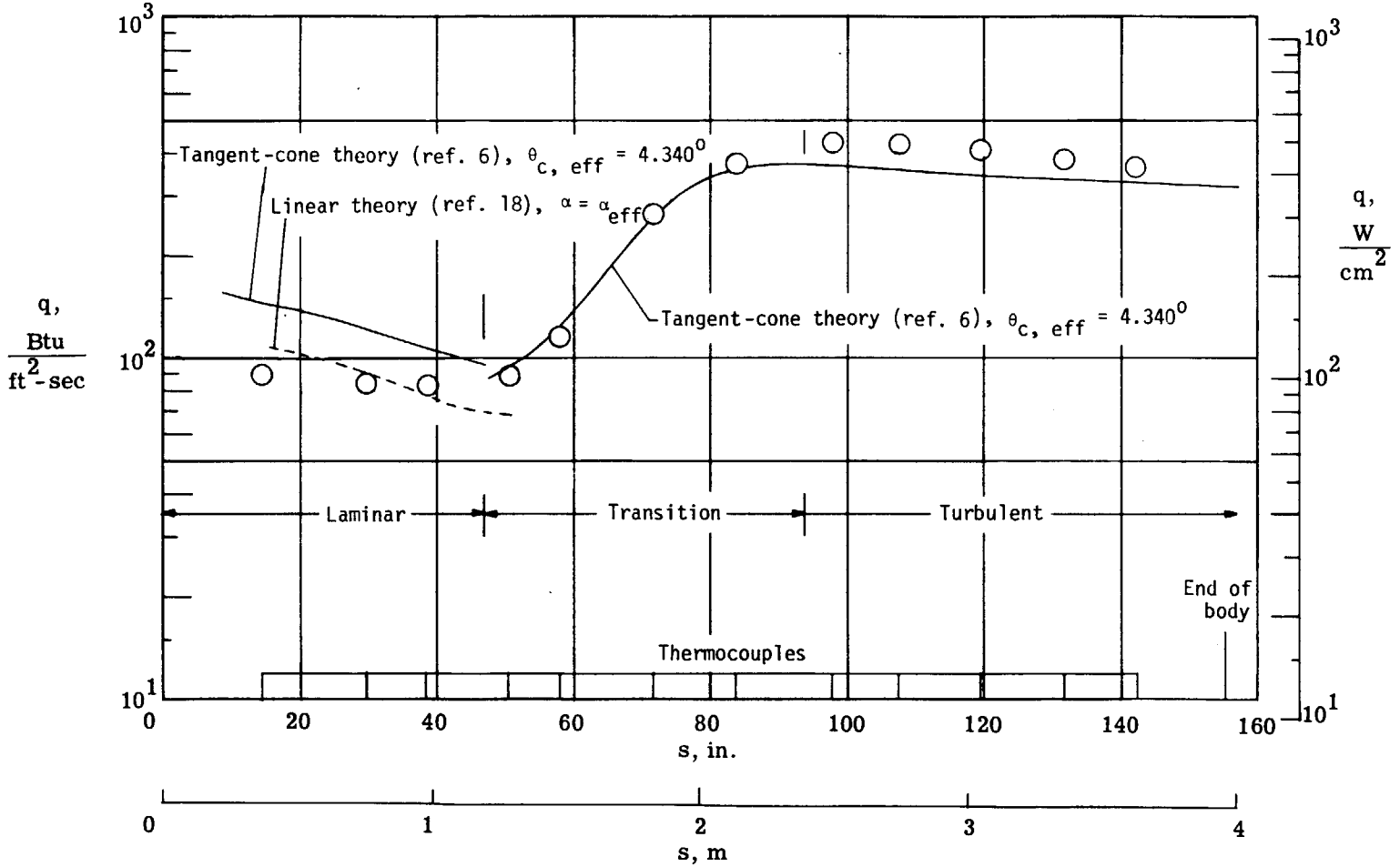

(g) h = 21.34 km (70 000 ft); V_∞ = 5.90 km/sec (19 367 ft/sec); r_n = 3.683 mm (0.145 in.).

Figure 2.- Continued.

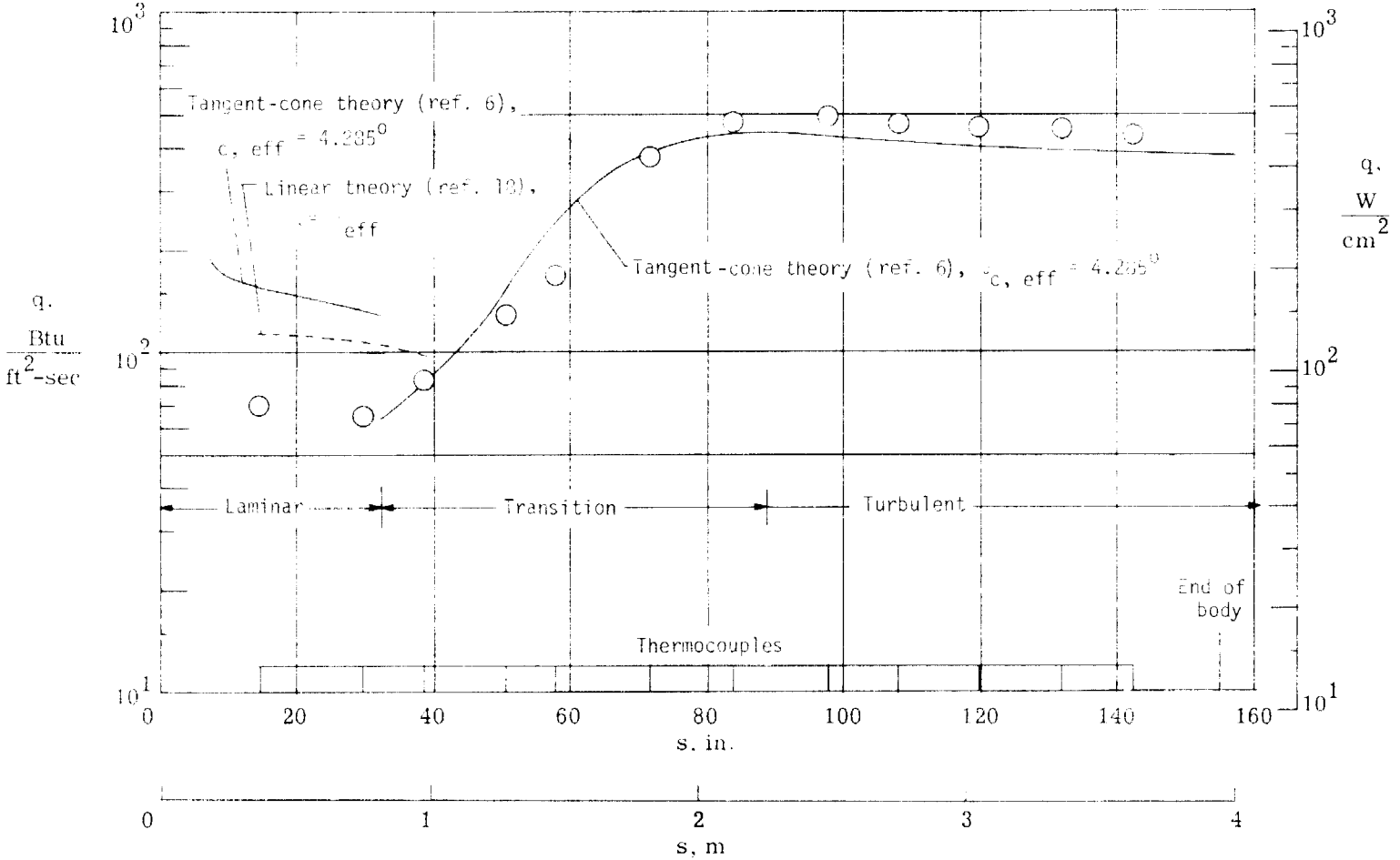

(h) h = 19.81 km (65 000 ft); V_∞ = 5.86 km/sec (19 215 ft/sec); r_n = 3.835 mm (0.151 in.).

Figure 2.- Continued.

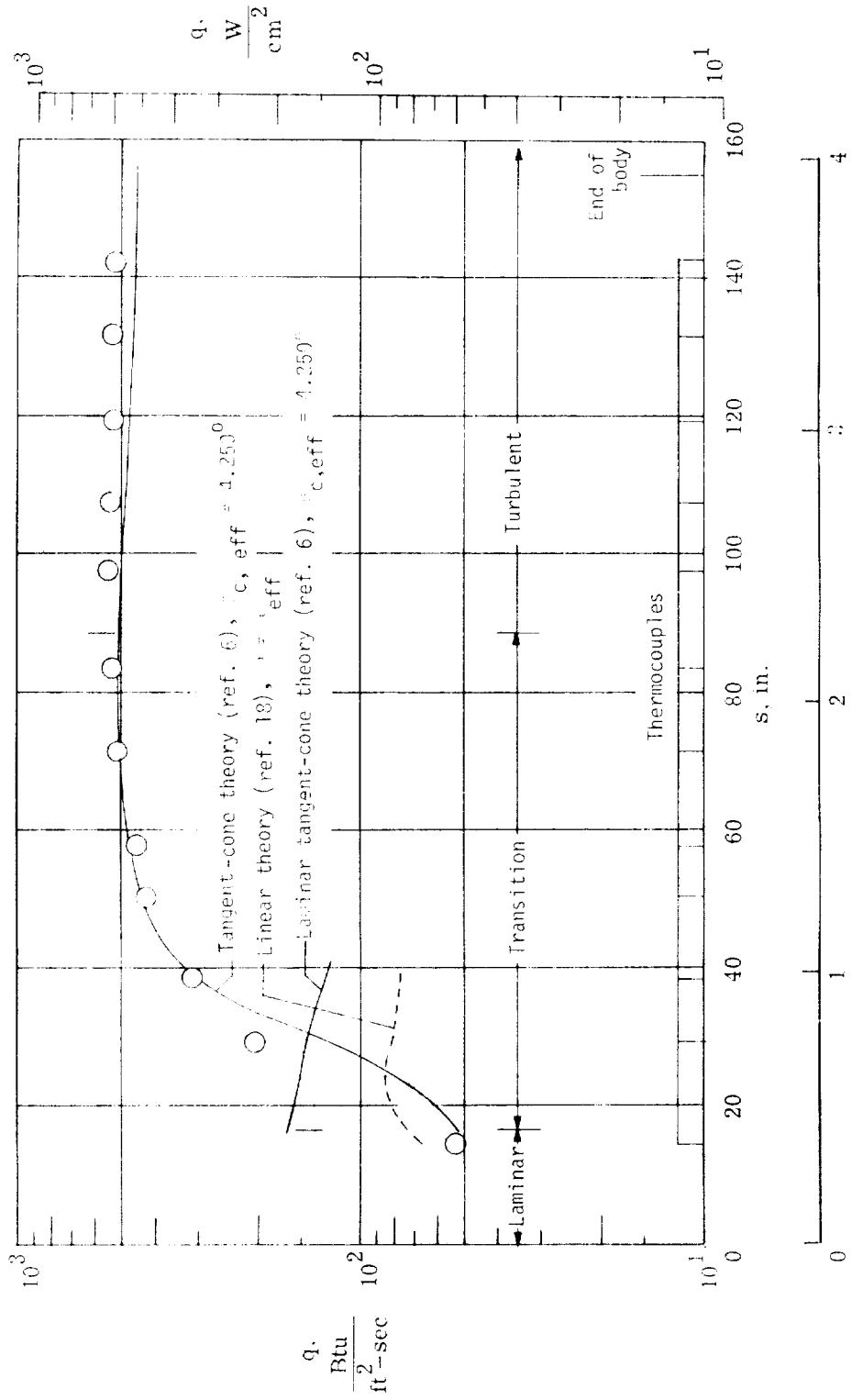

(i) h = 18.29 km (60 000 ft): V_∞ = 5.80 km/sec (19 018 ft/sec): r_n = 3.988 mm (0.157 in.).

Figure 2.- Continued.

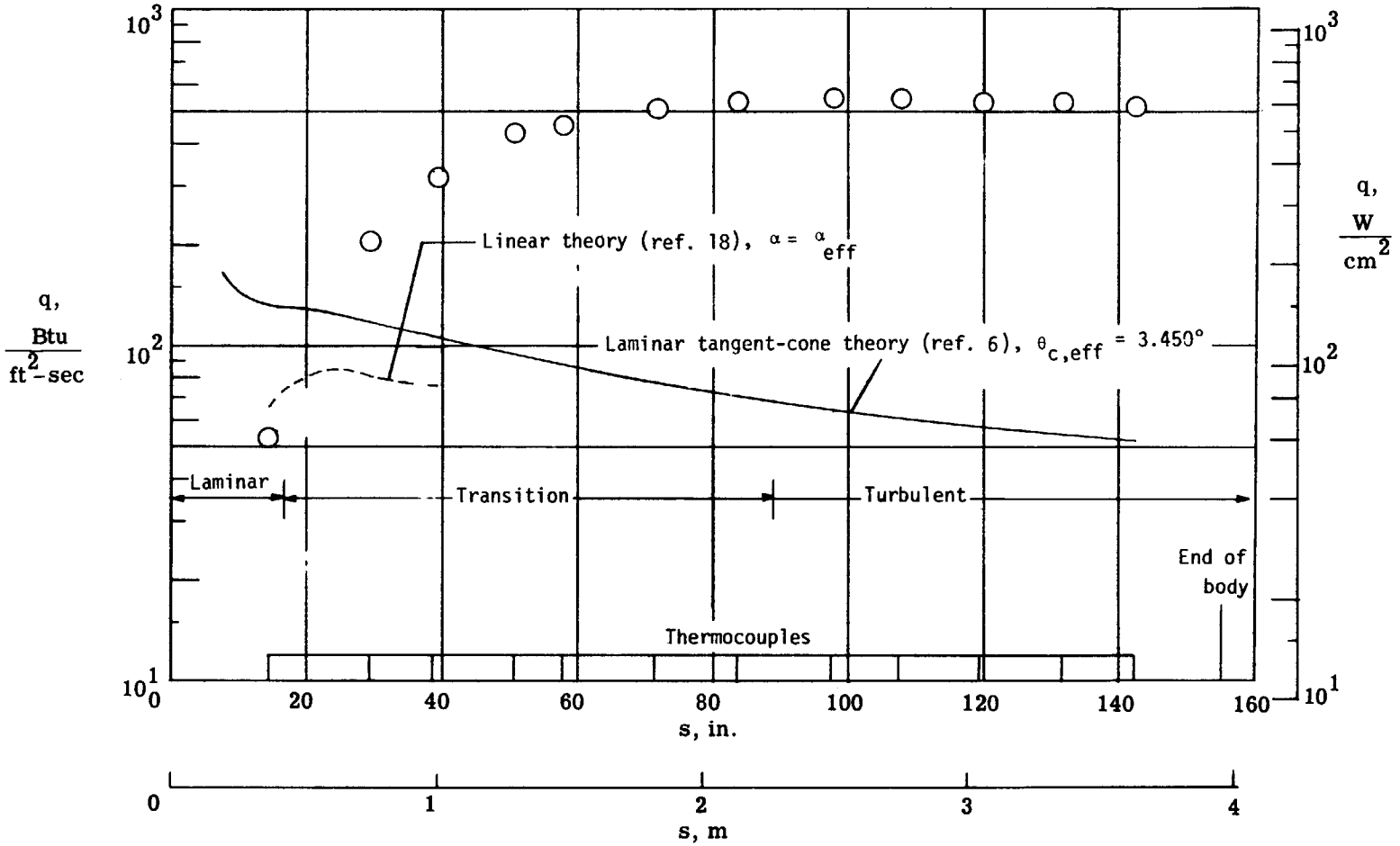

(j) h = 18.29 km (60 000 ft); V_∞ = 5.80 km/sec (19 018 ft/sec); r_n = 3.988 mm (0.157 in.).

Figure 2.- Concluded.

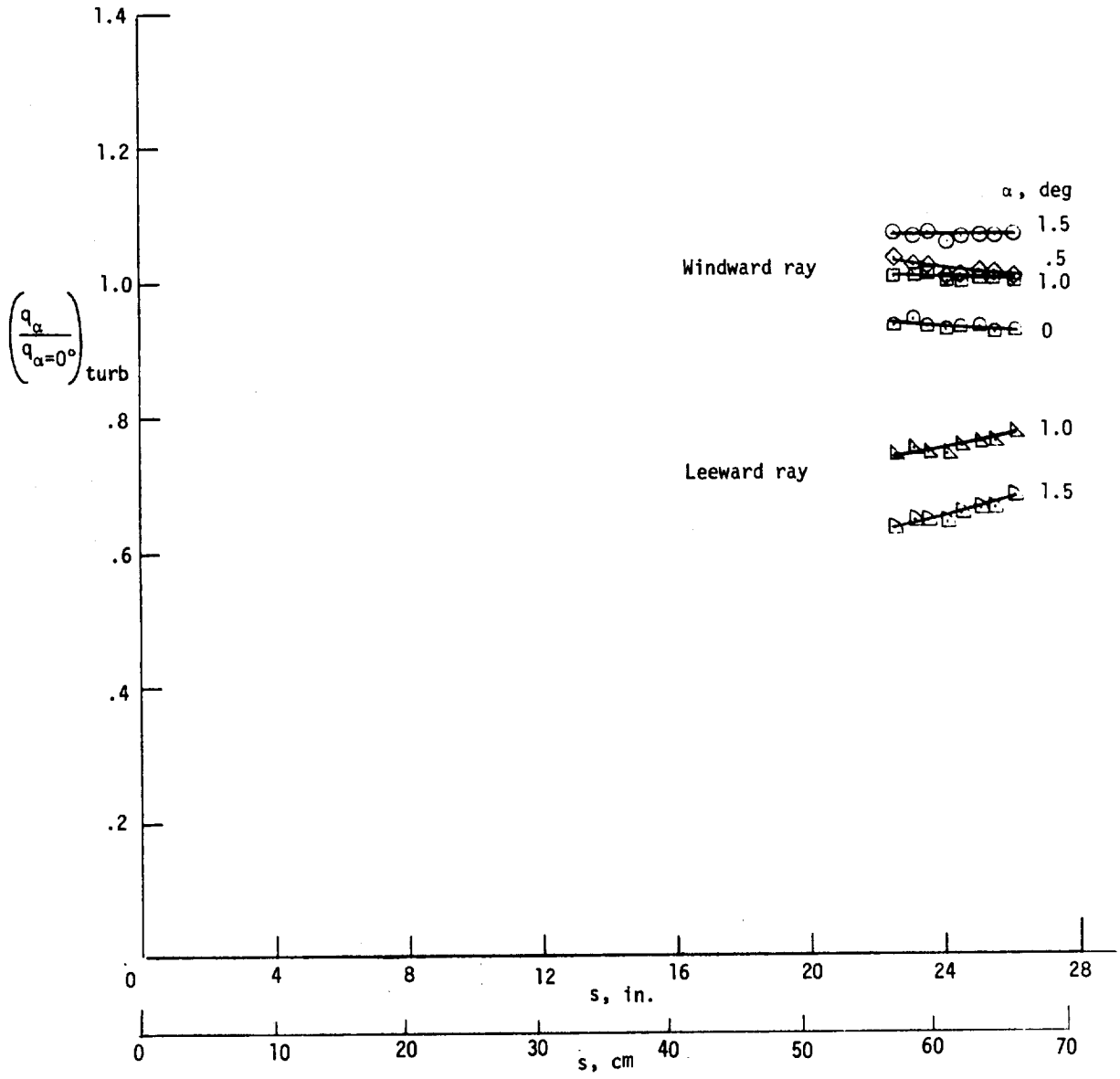

(a) Reentry F nose; $\phi = 0^o$; $r_n = 2.44$ mm (0.096 in.).

Figure 3.- Effect of angle of attack and nose configuration on longitudinal heating rates.

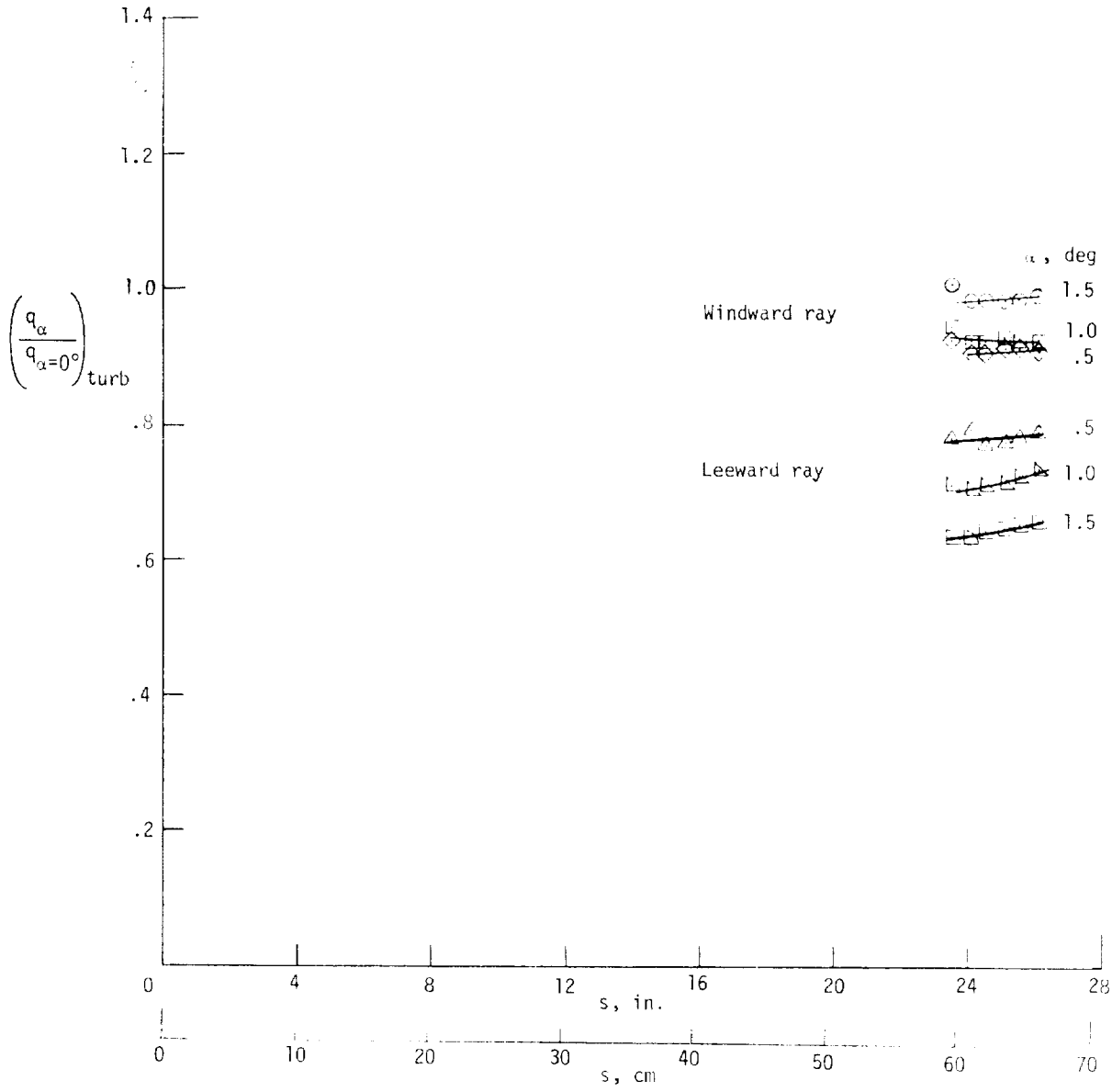

(b) Reentry F nose; $\phi = 10^{o}$; $r_n = 2.44$ mm (0.096 in.).

Figure 3.- Continued.

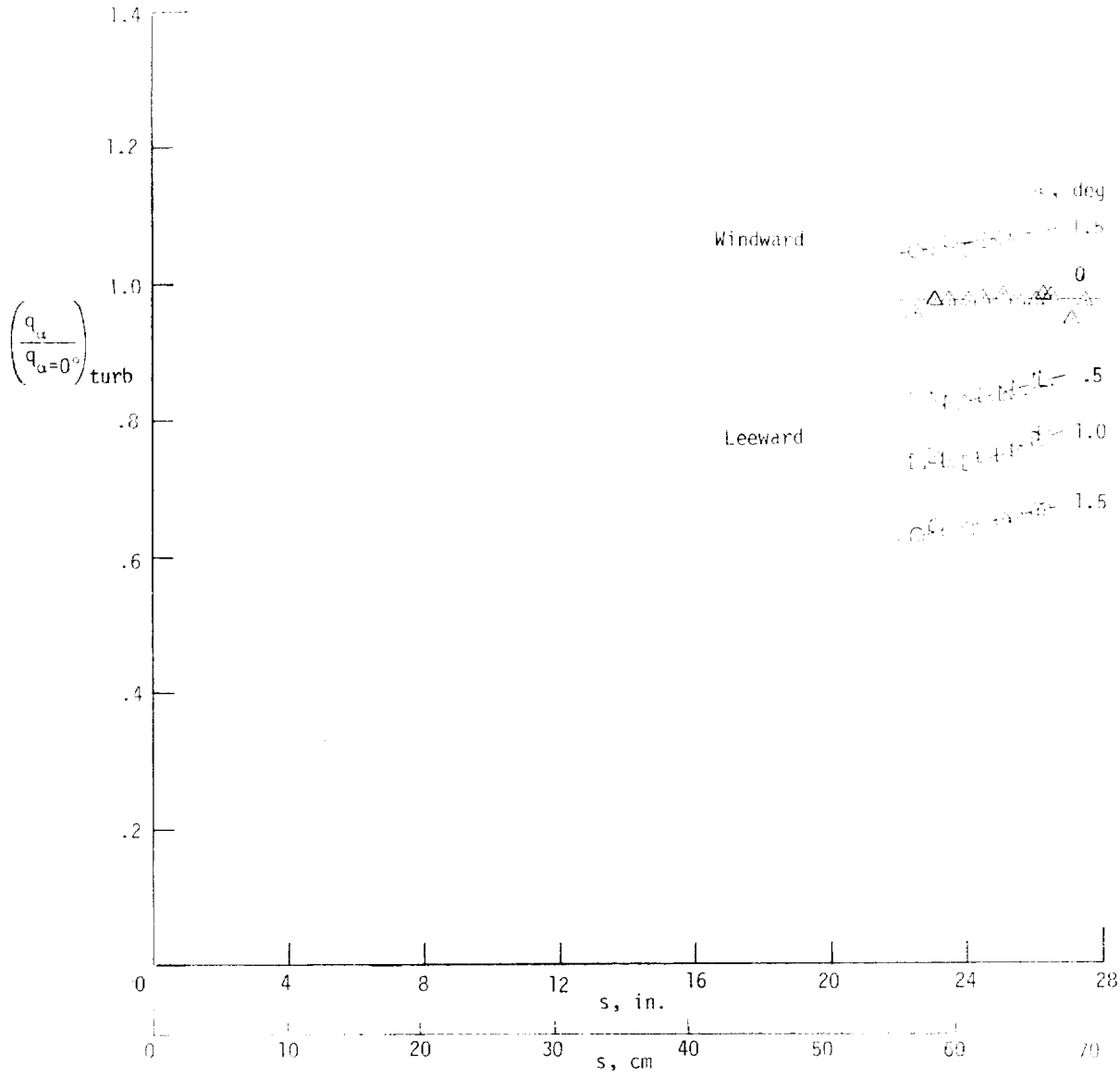

(c) Reentry F nose with forward-facing step; $\phi = 0^{o}$; $r_n = 2.44$ mm (0.096 in.).

Figure 3.- Continued.

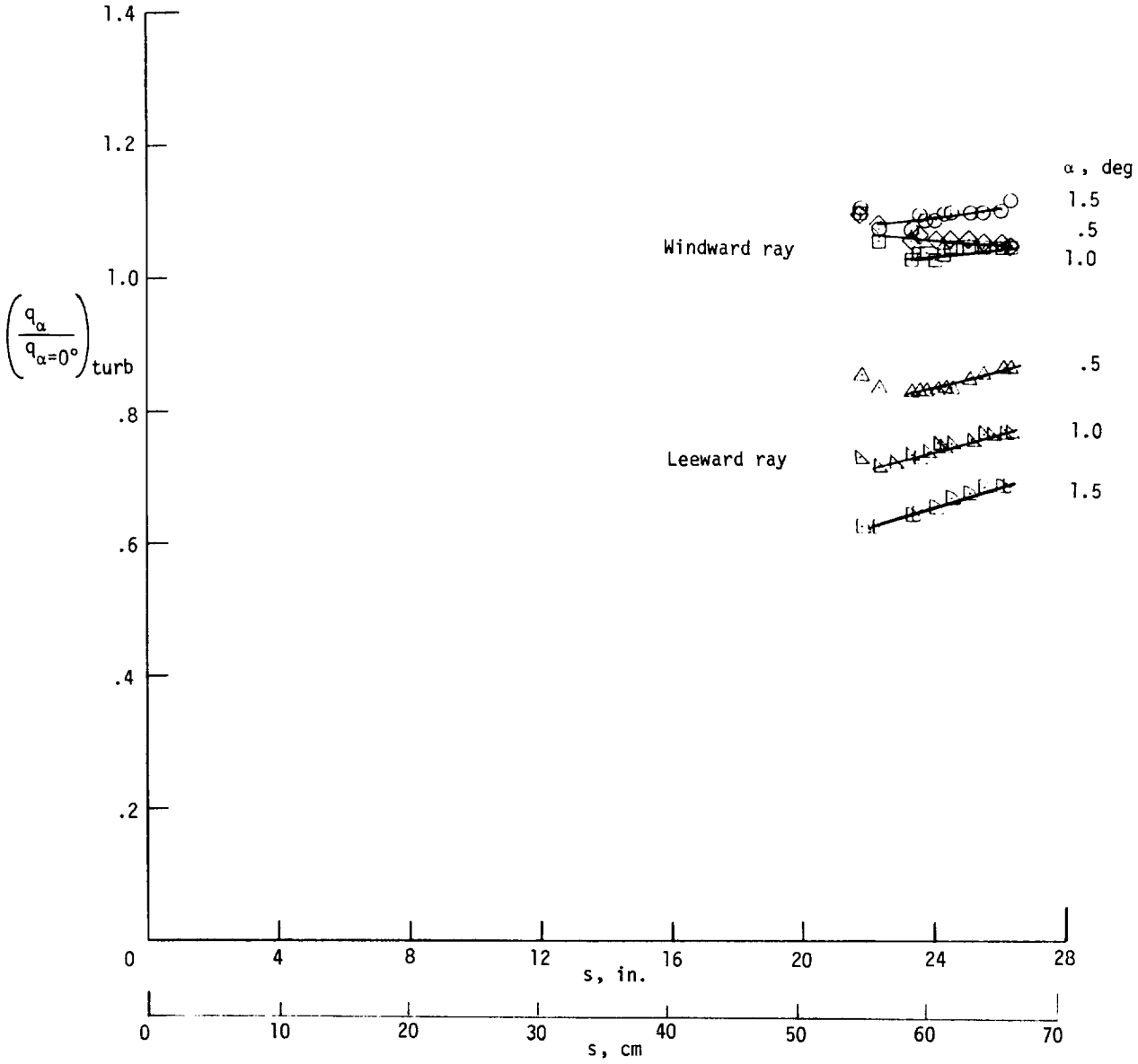

(d) Smooth nose; $\phi = 0^o$; $r_n = 2.54$ mm (0.10 in.).

Figure 3.- Continued.

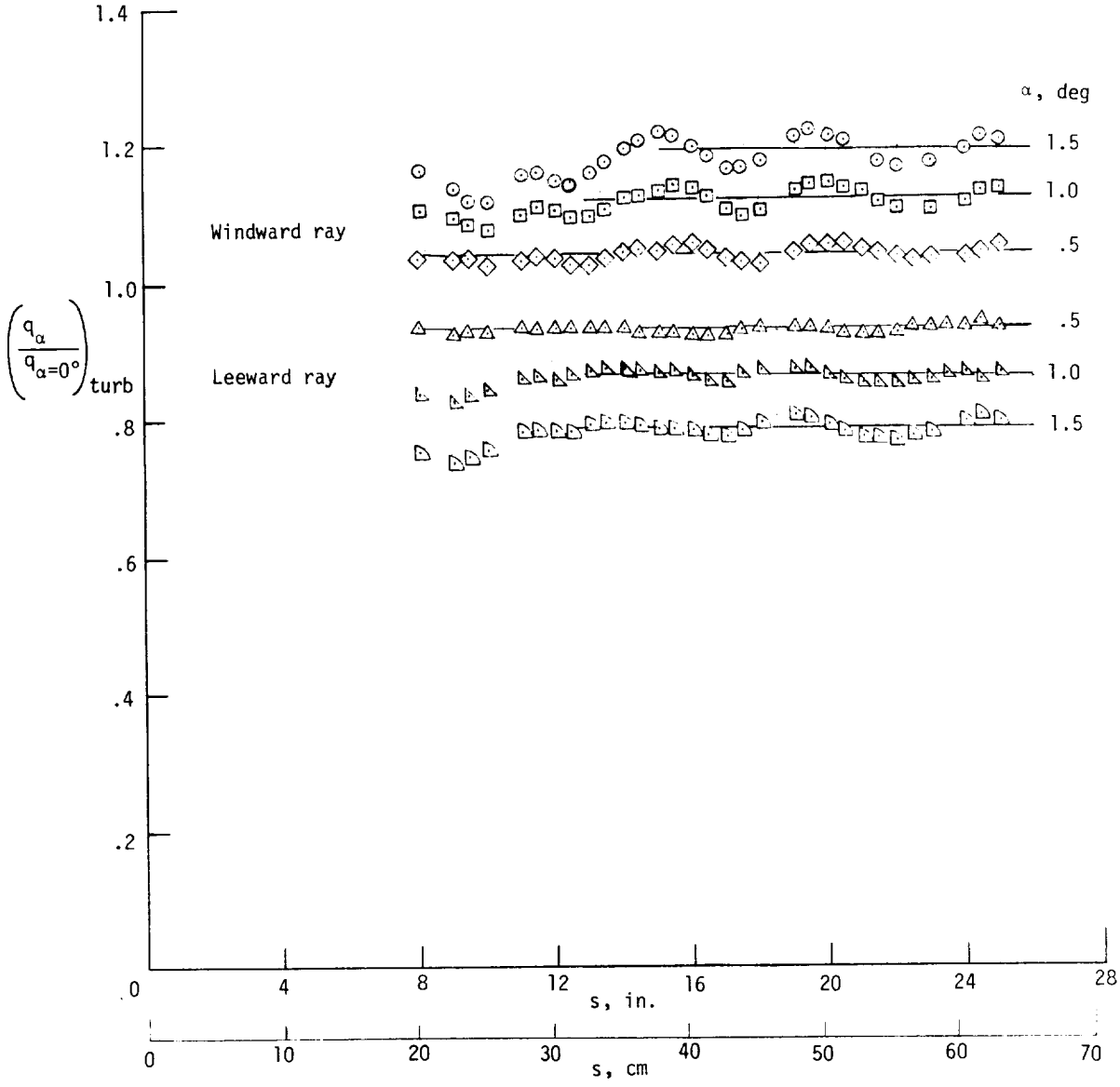

(e) Reentry F nose; $\phi = 0^o$; $r_n = 0.508$ mm (0.020 in.).

Figure 3.- Continued.

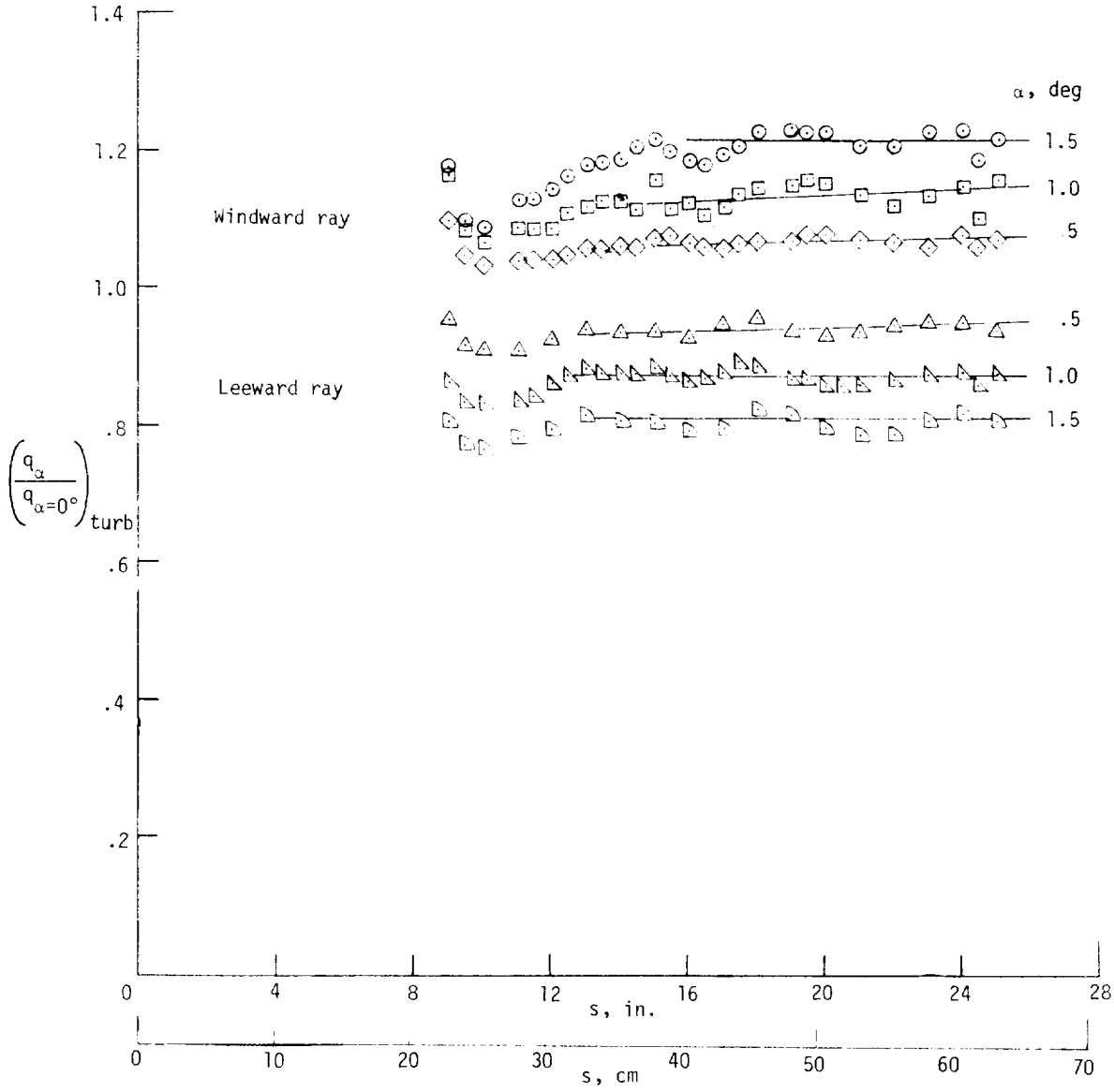

(f) Reentry F nose; $\phi = 10^{o}$; $r_n = 0.508$ mm (0.020 in.).

Figure 3.- Continued.

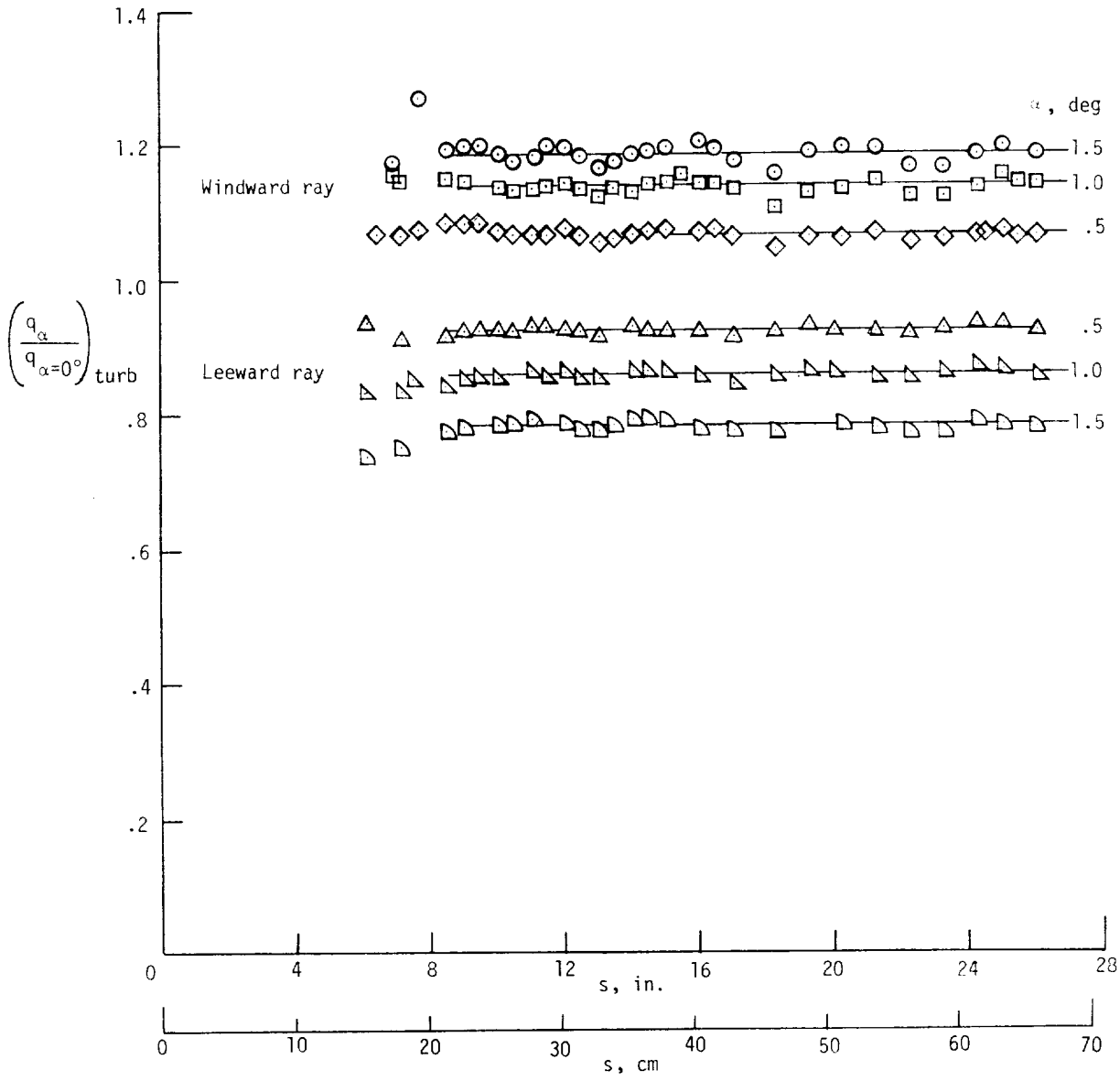

(g) Smooth nose; $\phi = 0^{o}$; $r_n = 0$.

Figure 3.- Concluded.

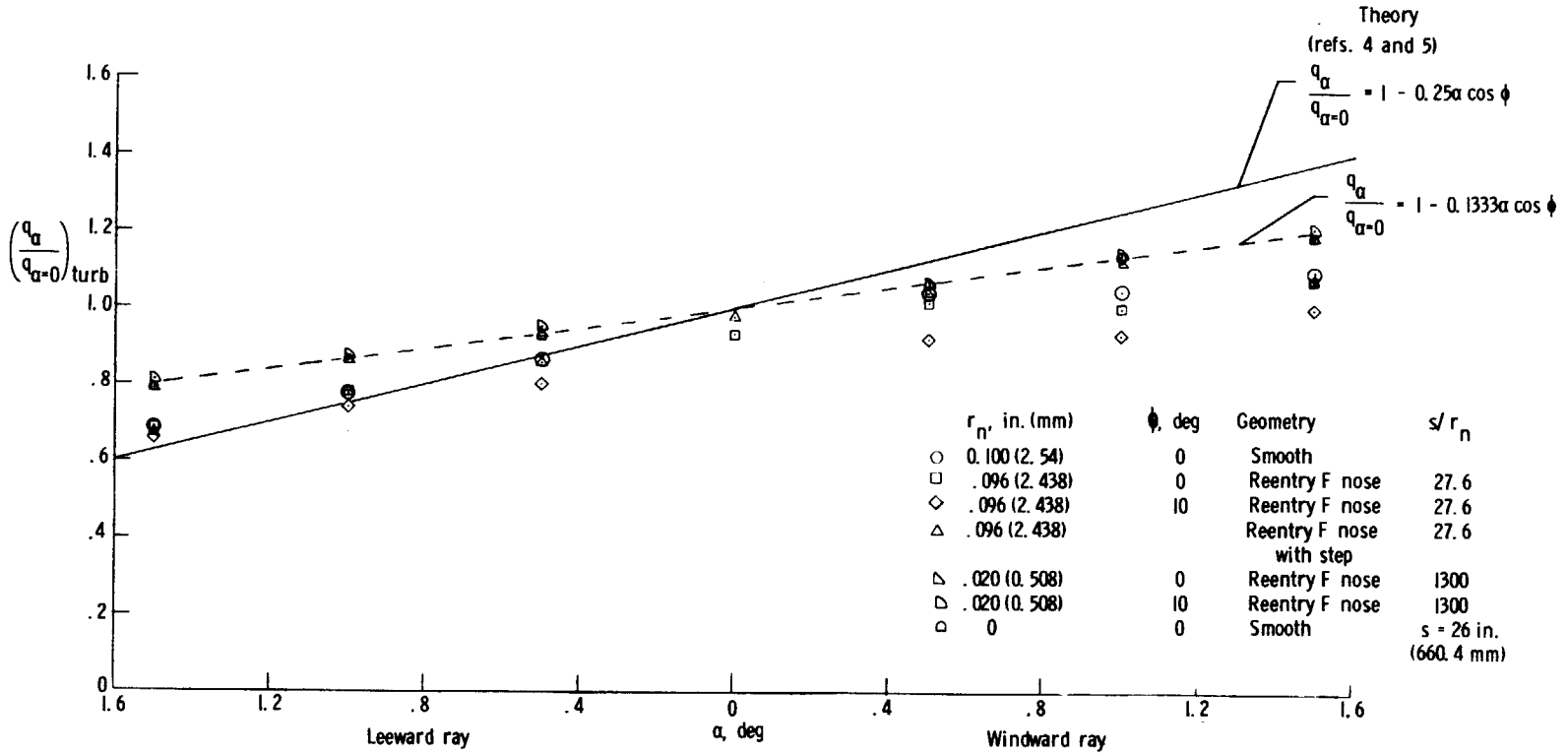

Figure 4.- Effect of angle of attack on turbulent heating rate for different nose shapes and roll angles.

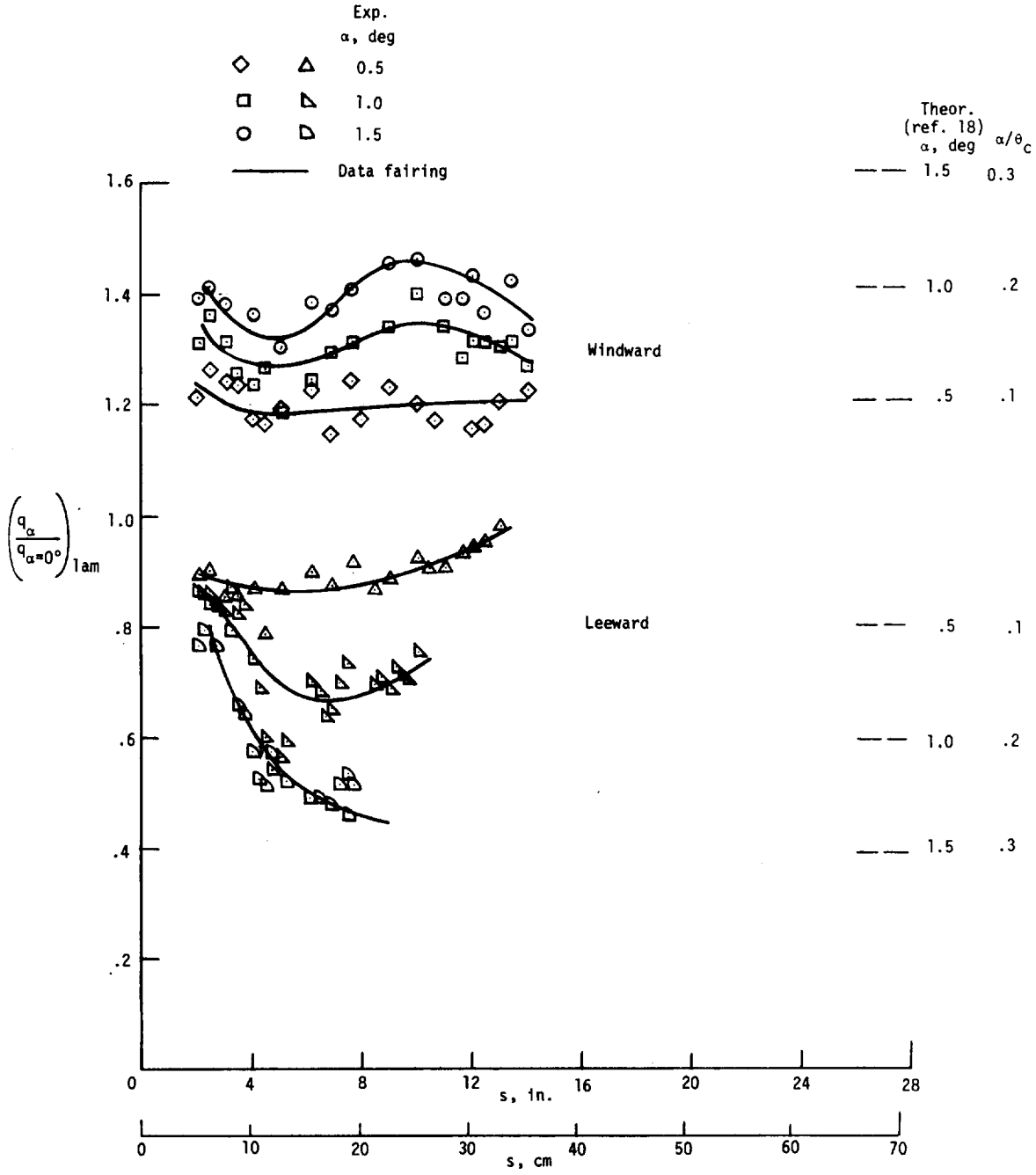

(a) Sharp nose (smooth surface); $\phi = 0^{o}$; $r_n = 0$.

Figure 5.- Wind-tunnel laminar heating rates.

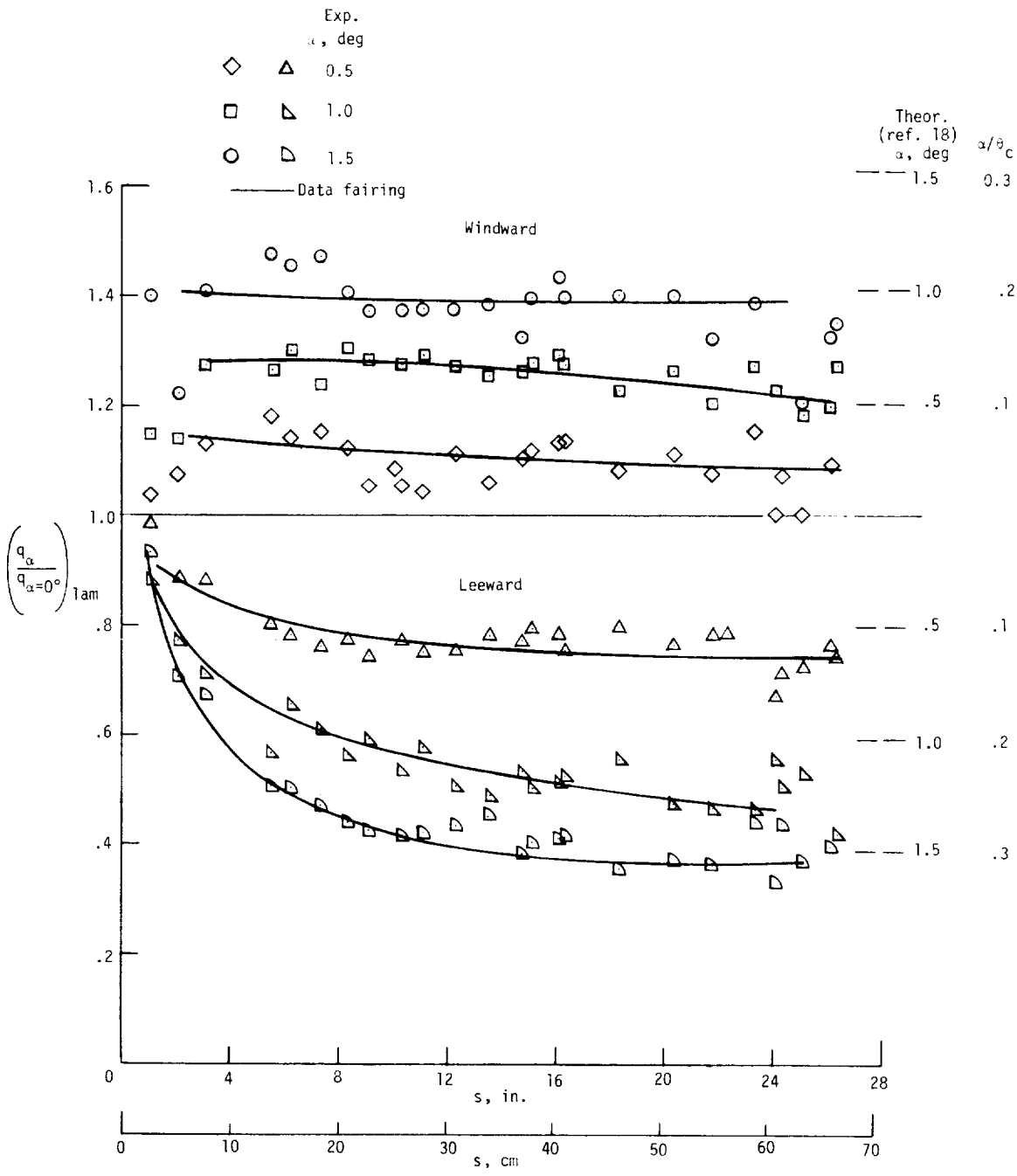

(b) Blunt nose (smooth surface); $\phi = 0^{o}$; $r_n = 2.54$ mm (0.10 in.)

Figure 5.- Continued.

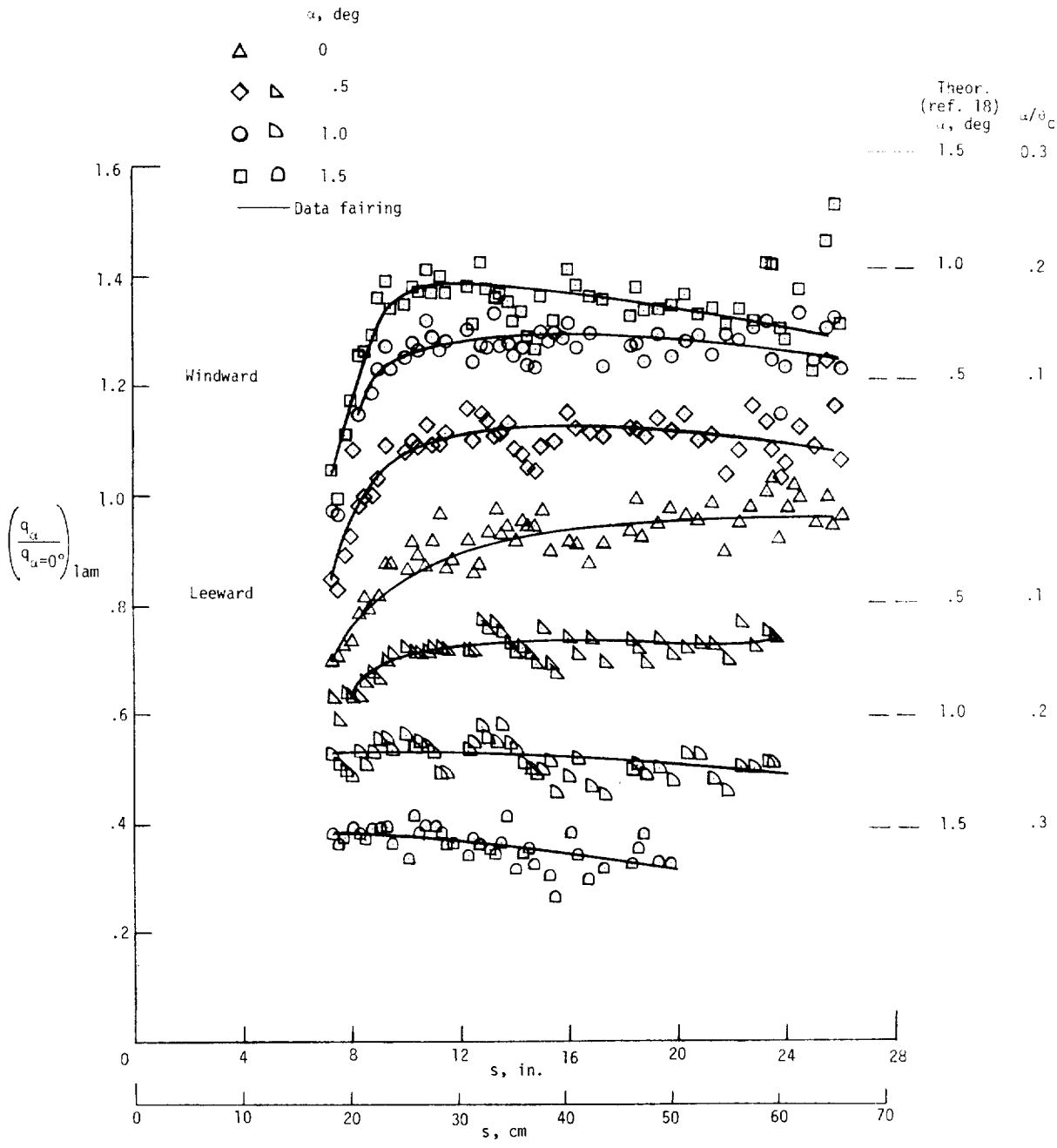

(c) Reentry F nose (step gap); $\phi = 0^{o}$; $r_n = 2.44$ mm (0.096 in.).

Figure 5.- Continued.

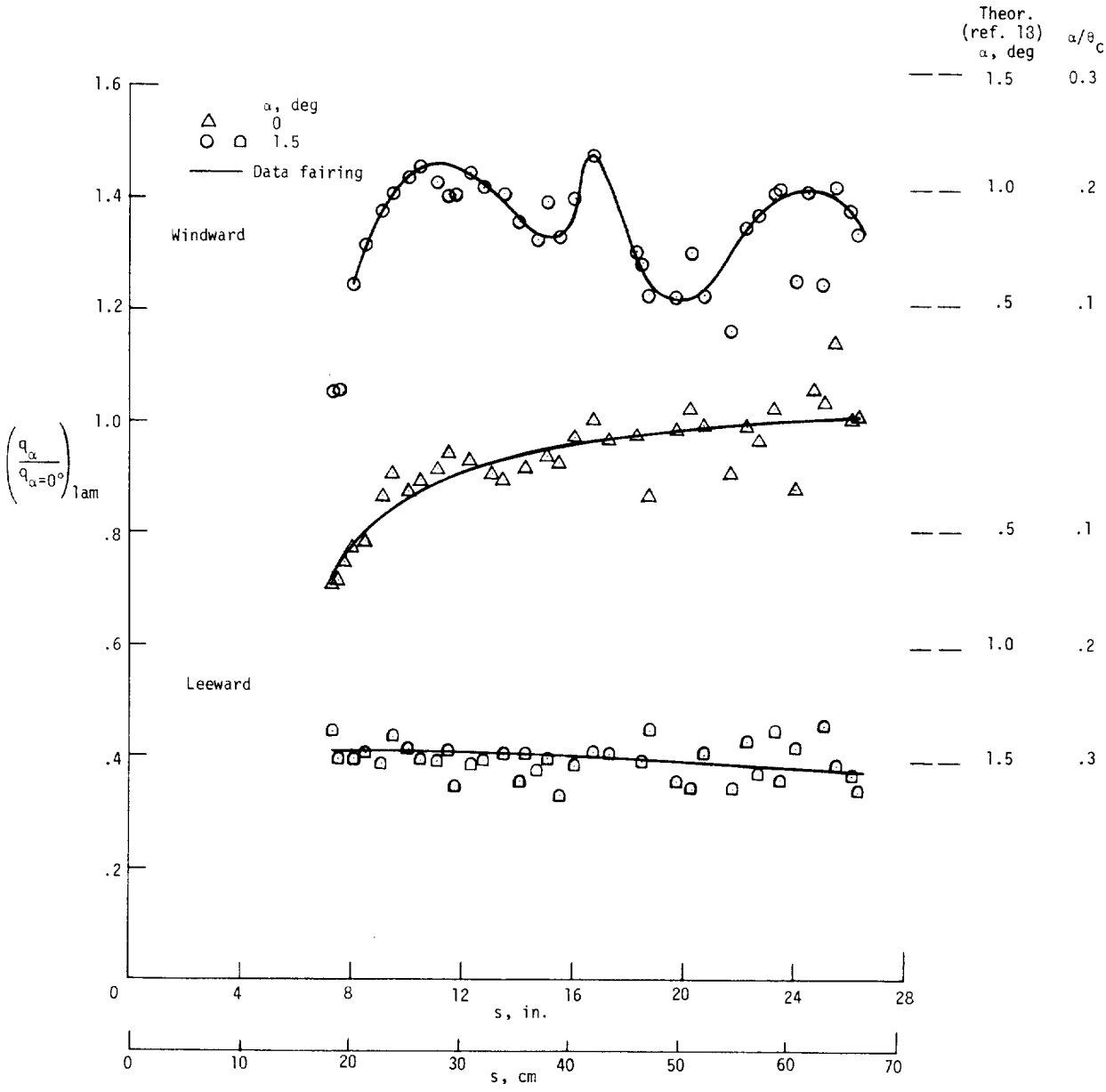

(d) Reentry F nose (step gap); $\phi = 10^o$; $r_n = 2.44$ mm (0.096 in.).

Figure 5.- Continued.

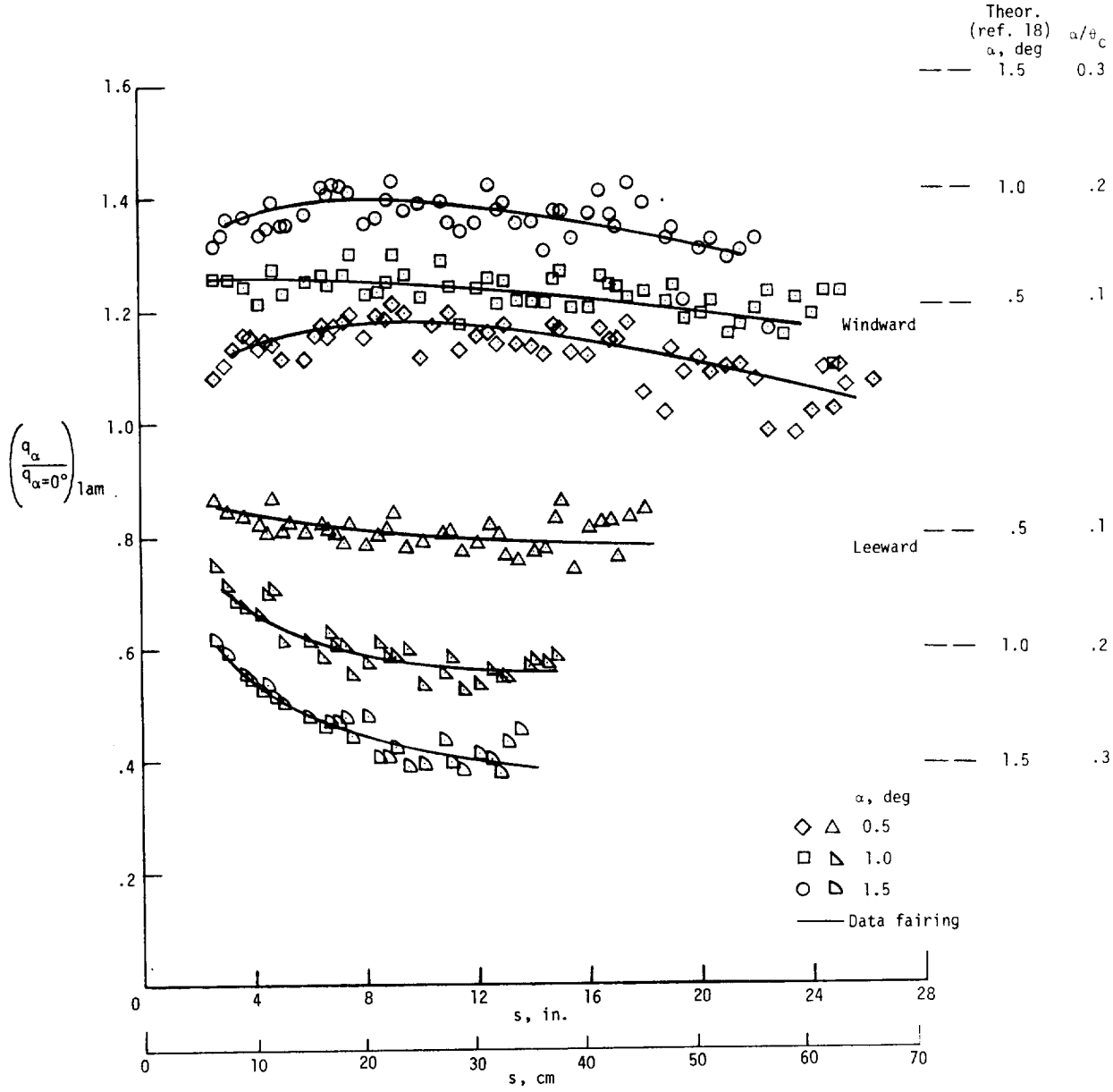

(e) Reentry F nose (step gap); $\phi = 0^o$; $r_n = 0.508$ mm (0.020 in.).

Figure 5.- Continued.

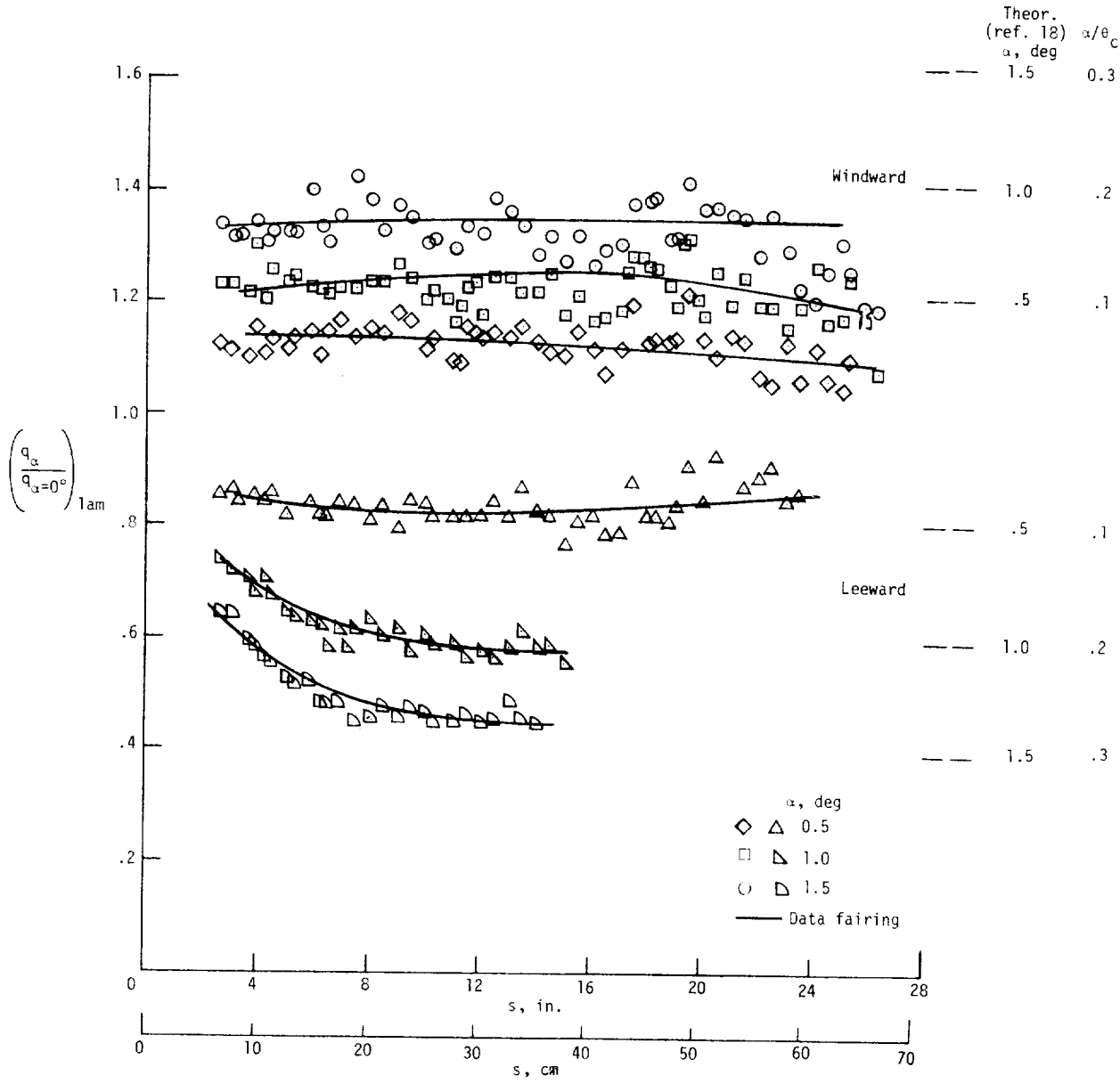

(f) Reentry F nose (step gap); $\phi = 10^{o}$; $r_n = 0.508$ mm (0.020 in.).

Figure 5.- Continued.

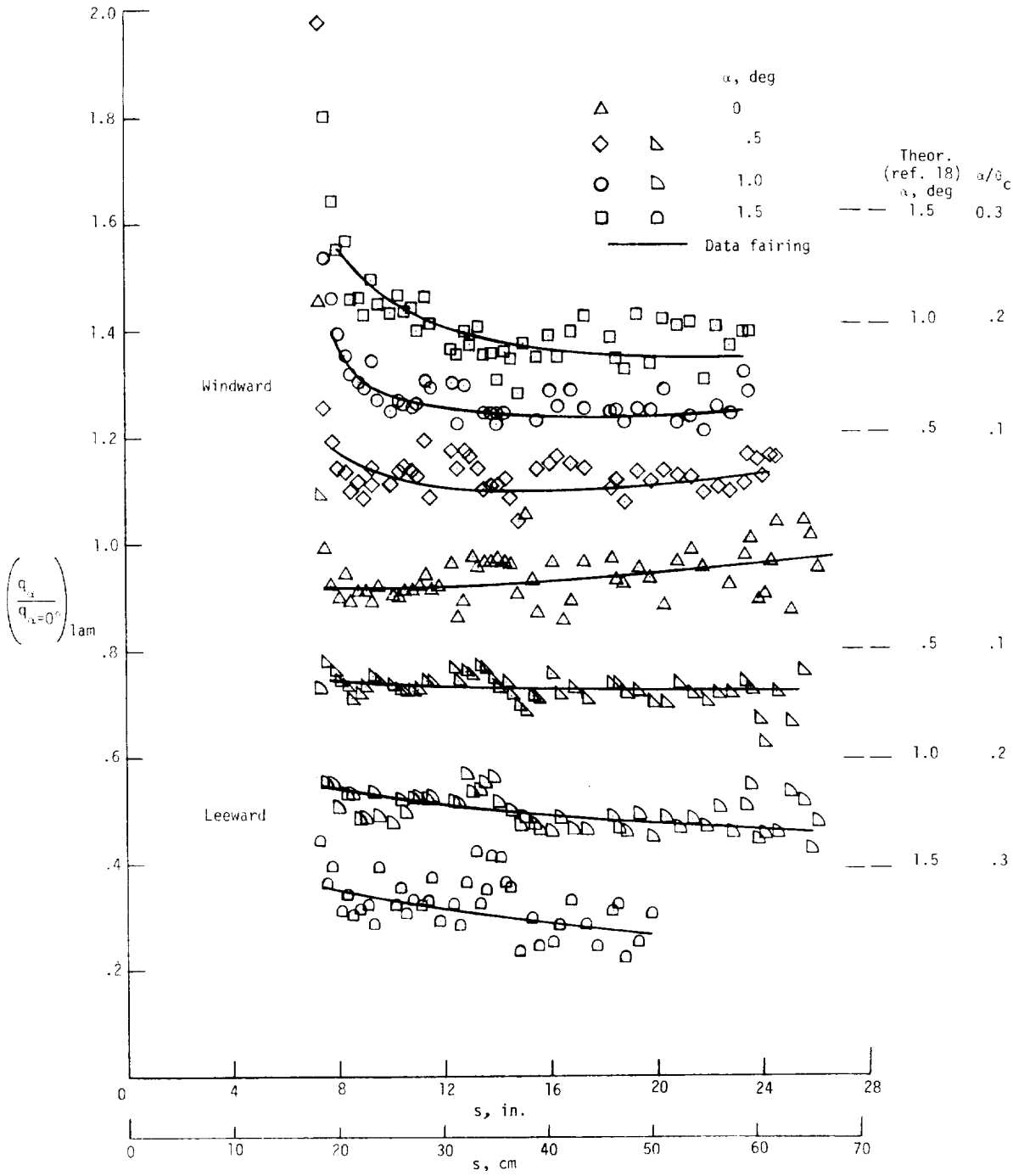

(g) Reentry F nose with forward-facing step; $\phi = 0^{o}$; $r_n = 2.44$ mm (0.096 in.).

Figure 5.- Concluded.

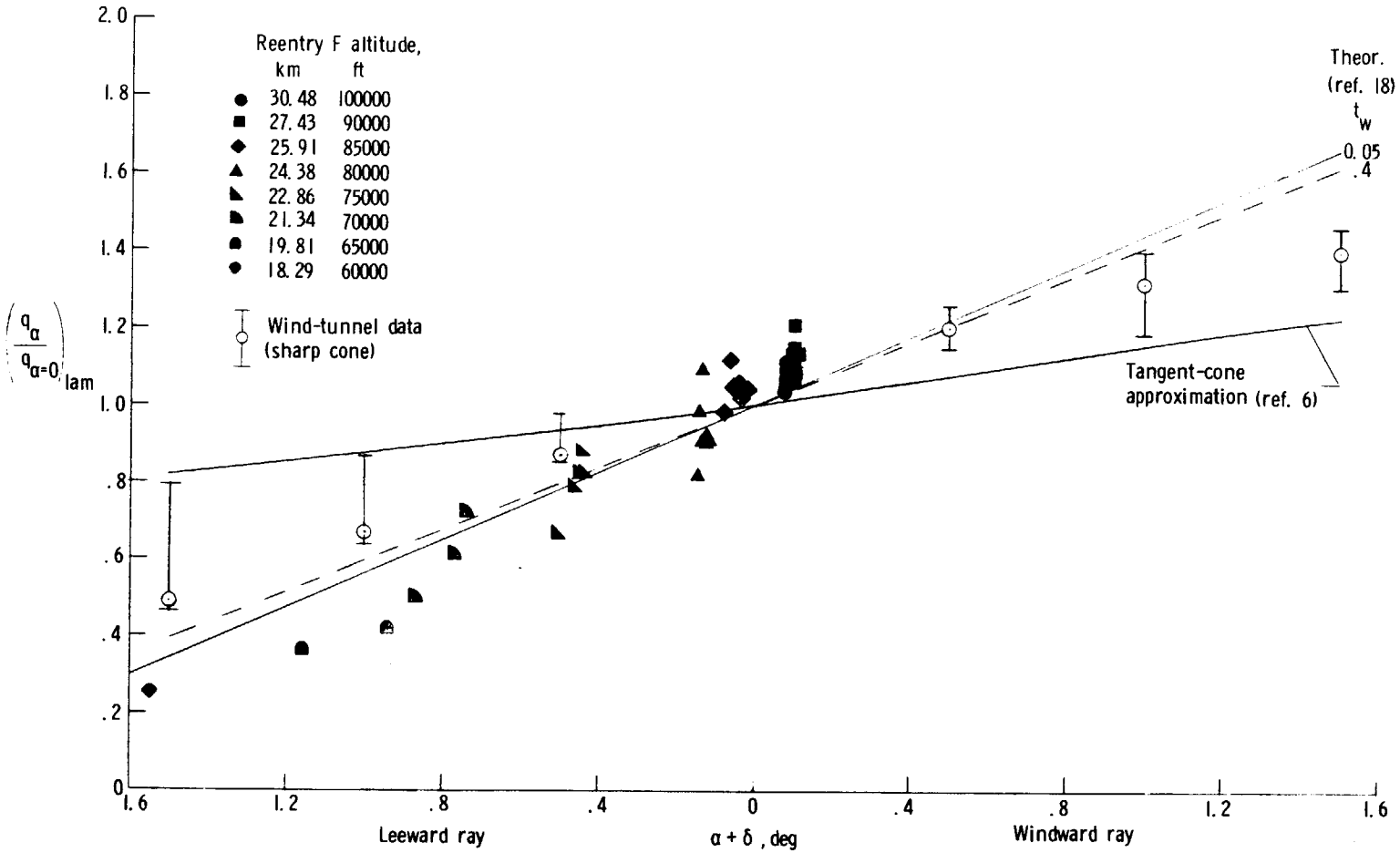

Figure 6.- Laminar heating-rate variation with flow deflection angle for sharp cone.

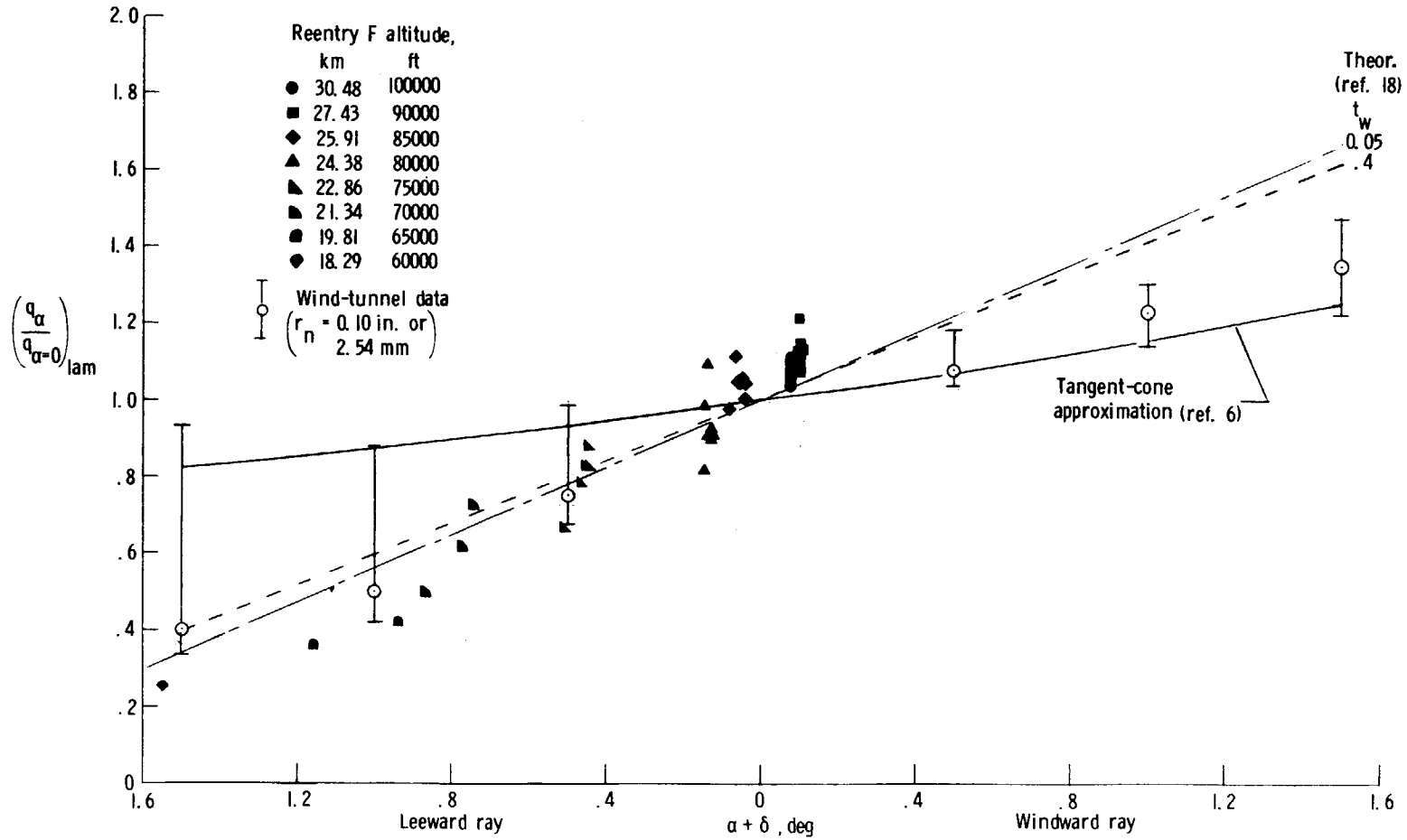

Figure 7.- Laminar heating-rate variation with flow deflection angle for smooth cone. r_n = 2.54 mm (0.10 in.).

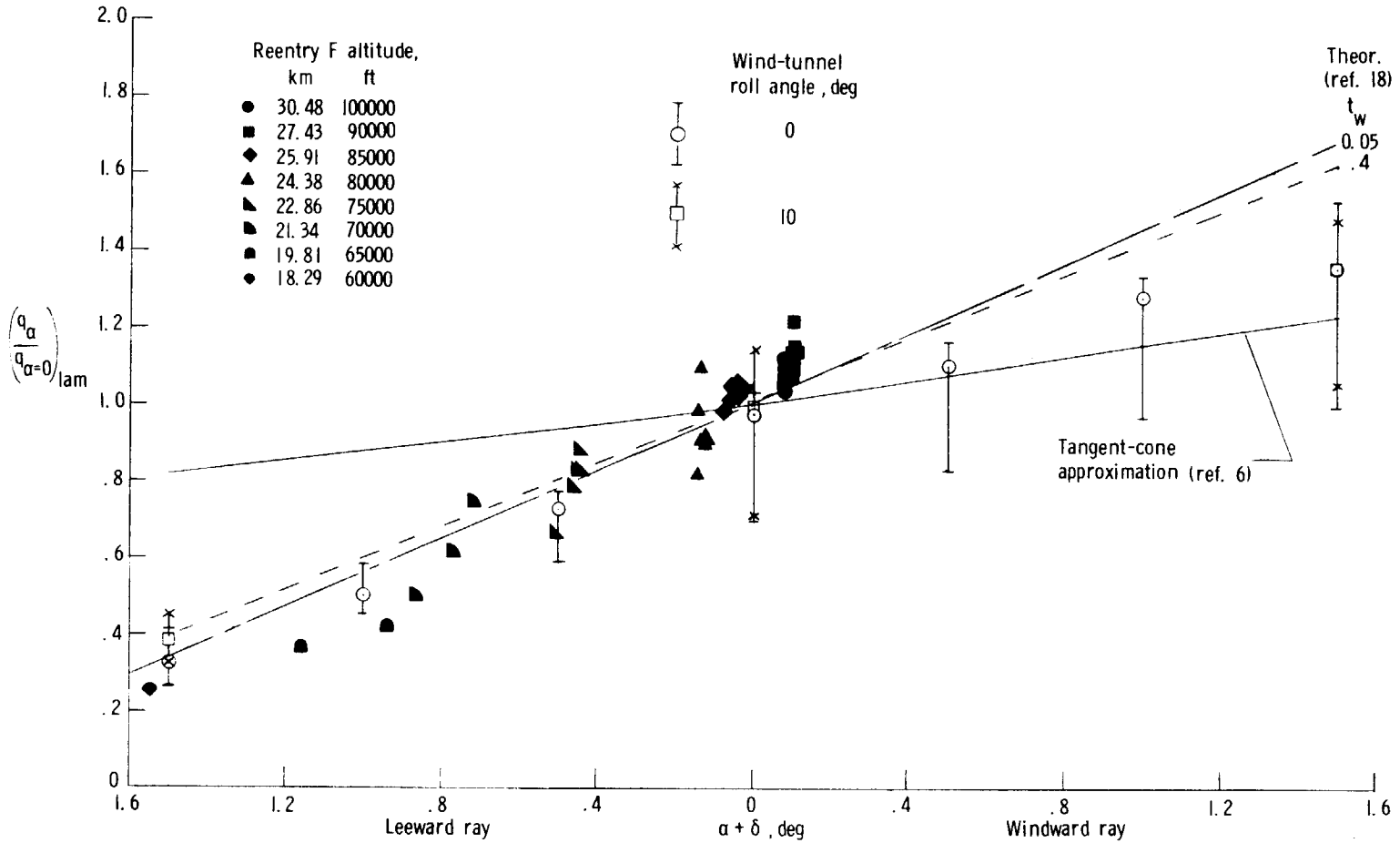

(a) r_n = 2.44 mm (0.096 in.).

Figure 8.- Heating-rate variation with flow deflection angle for Reentry F nose.

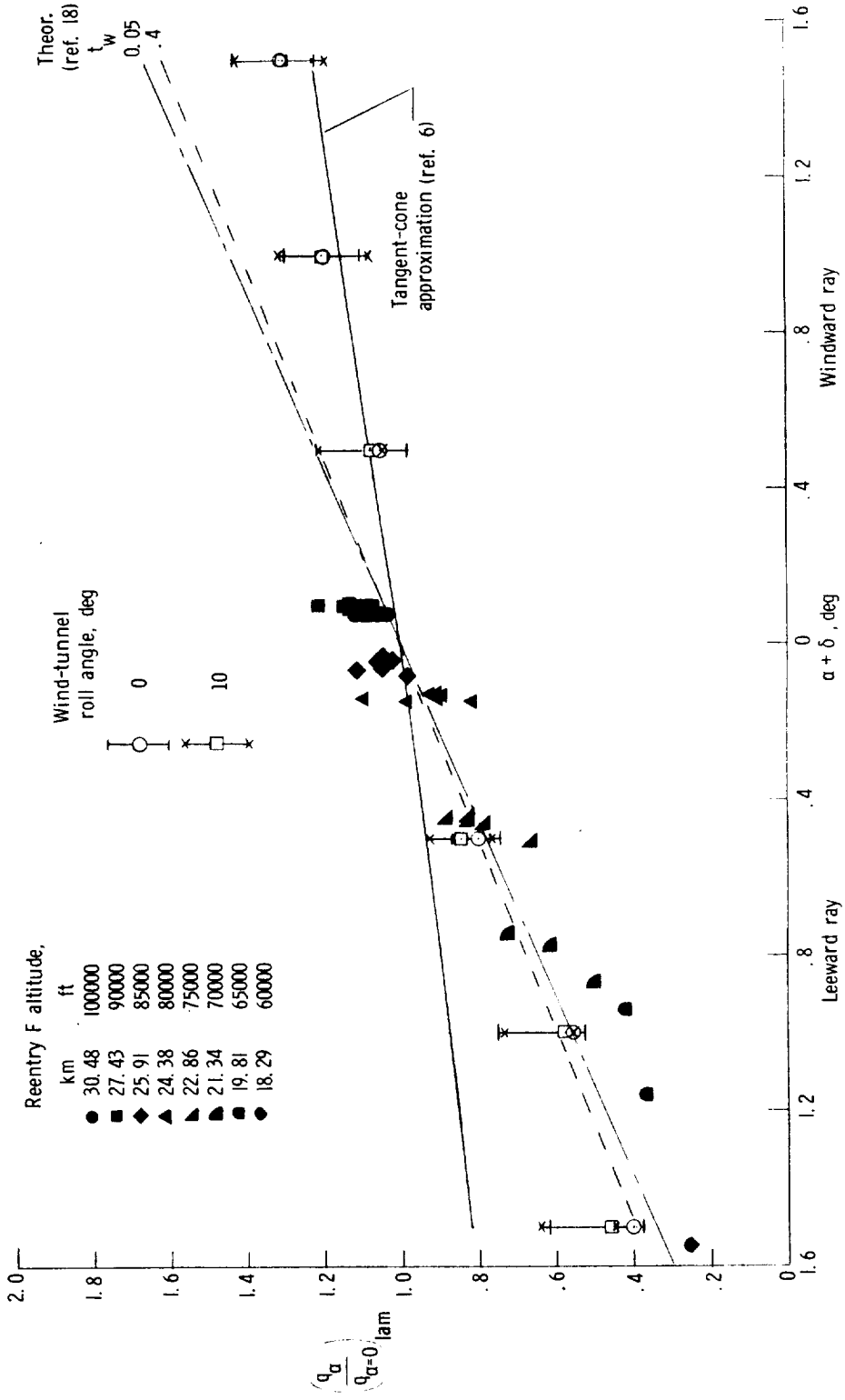

(b) $r_n = 0.508$ mm (0.020 in.).

Figure 8.- Continued.

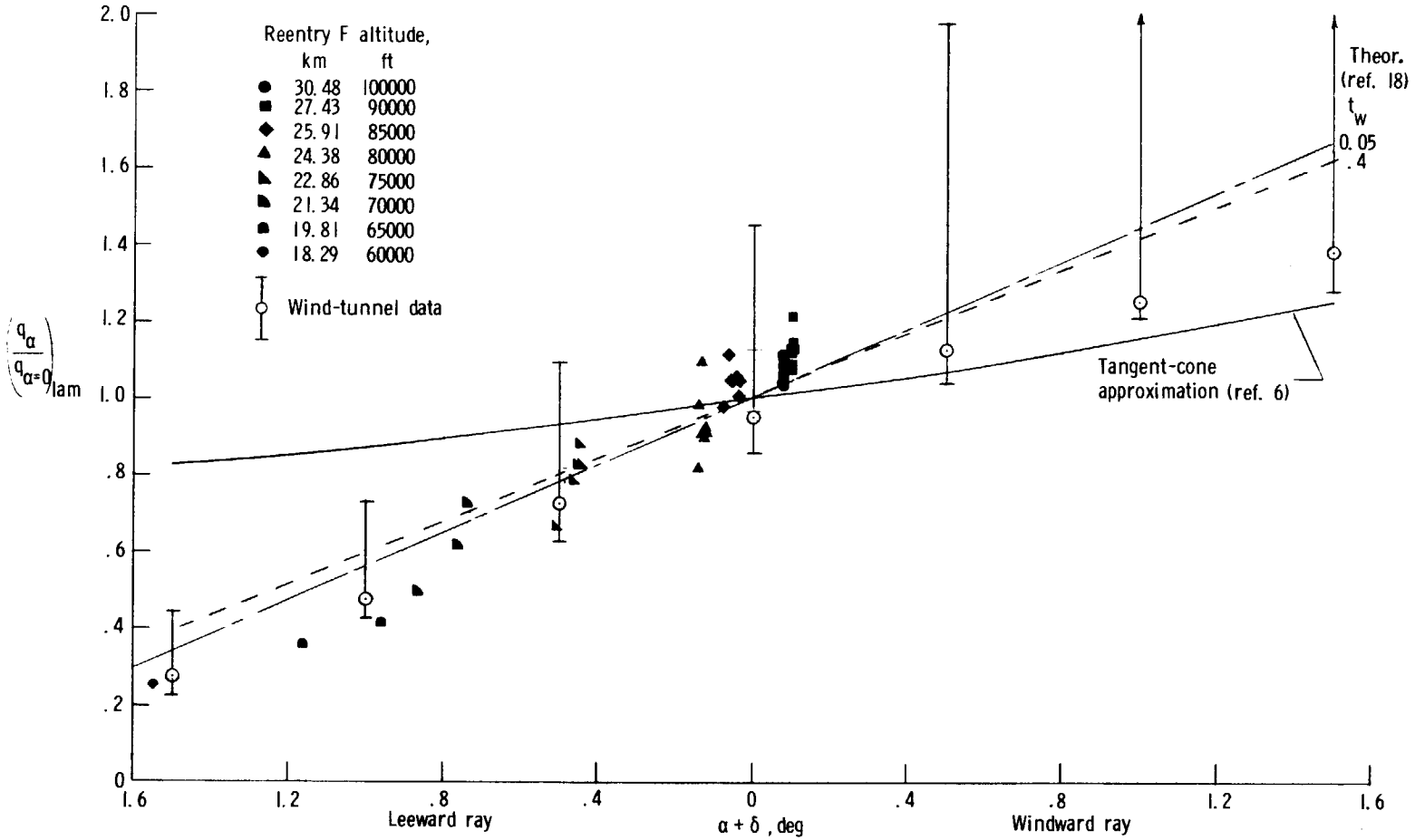

(c) r_n = 2.44 mm (0.096 in.); forward-facing step.

Figure 8.- Concluded.

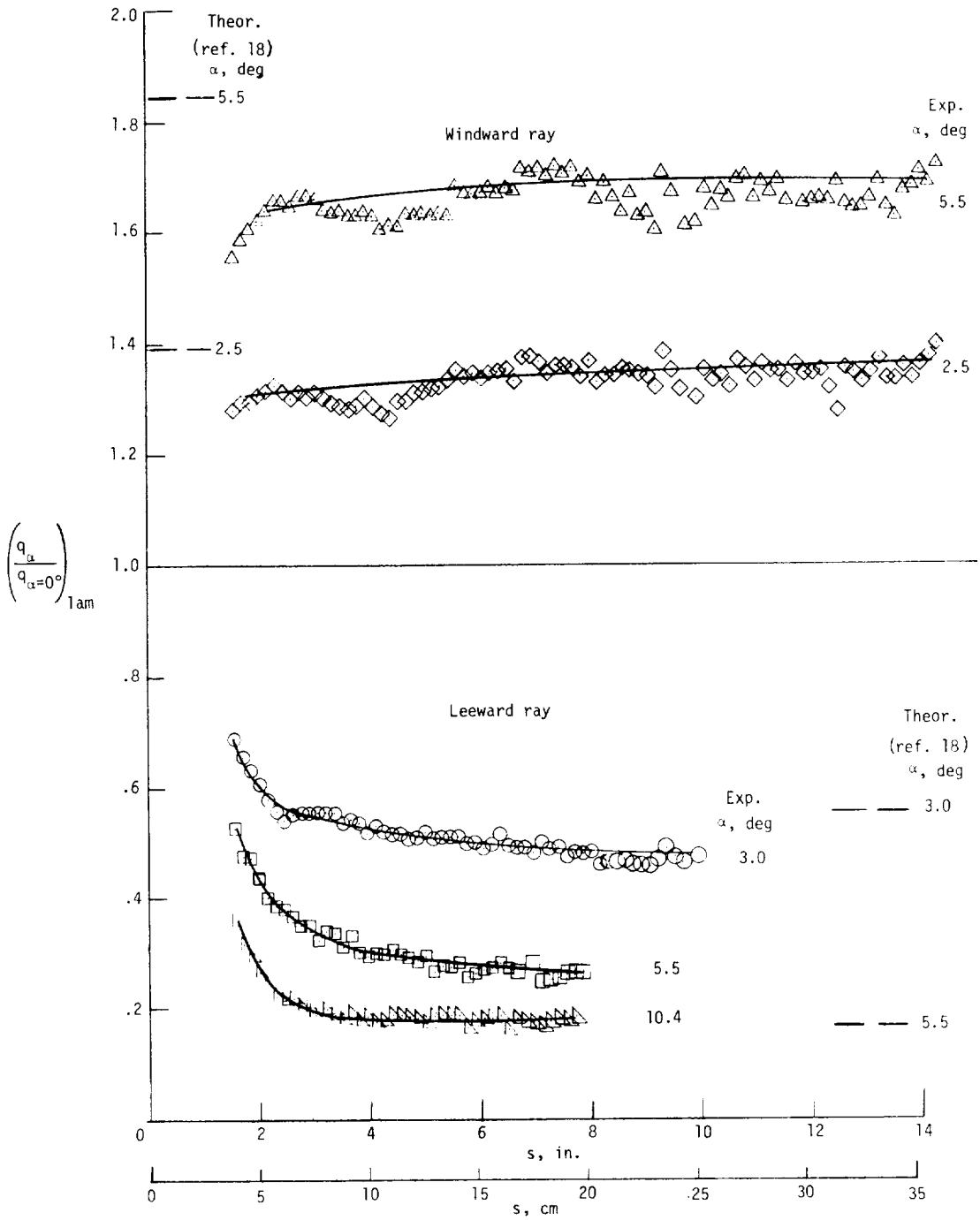

Figure 9.- Laminar heat transfer to sharp 10° half-angle cone at angle of attack. $R_\infty = 5.25 \times 10^6$ per meter (1.6×10^6 per foot).